ADDIS ABABA UNIVERSITY
SCHOOL OF EARTH SCIENCES

REMOTE SENSING AND GIS BASED DETERMINATION OF EVAPOTRANSPIRATION OF LAKE TANA BASIN, NORTH ETHIOPIA

Thesis submitted for Partial Fulfilment of the Requirements of Master of Science Degree in Remote Sensing and Geographical Information Systems (GIS), School of Graduate Studies, Addis Ababa University

By:
Yalew Bizu Abiy

Advisor:
Dr. K. V. Suryabhagavan
School of Earth Sciences

June, 2015

Addis Ababa, Ethiopia

REMOTE SENSING AND GIS BASED DETERMINATION OF EVAPOTRANSPIRATION OF LAKE TANA BASIN, NORTH ETHIOPIA

Thesis submitted for Partial Fulfilment of the Requirements of Master of Science Degree in Remote Sensing and Geographical Information Systems (GIS), School of Graduate Studies, Addis Ababa University

By:
Yalew Bizu Abiy

Advisor:
Dr. K. V. Suryabhagavan
School of Earth Sciences

June, 2015

Addis Ababa, Ethiopia

REMOTE SENSING AND GIS BASED DETERMINATION OF EVAPOTRANSPIRATION OF LAKE TANA BASIN, NORTH ETHIOPIA

Yalew Bizu Abiy

Thesis Submitted to School of Earth Sciences in Partial Fulfilment of the Requirements for the Degree of Master of Science in Remote Sensing and Geographic Information Systems (GIS).

Approved by Board of Examiners	Signature
Dr. Suryabhagavan (PhD)	
Chairman	_____
Dr. Getachew B.	
Examiner	_____
Dr. Dessie N.	
Examiner	_____
Dr. Suryabhagavan (PhD)	
Advisor	_____

June, 2015

C E R T I F I C A T E

This is to certify that the dissertation entitled **"Remote Sensing and GIS Based Determination of Evapotranspiration of Lake Tana Basin, Northwest Ethiopia"** is a field work carried out by Yalew Bizu Abiy under my guidance and supervision. This is the actual work done by Yalew Bizu for the partial fulfilment of the award of the Degree of Master of Science in Remote Sensing and GIS from Addis Ababa University, Addis Ababa, Ethiopia.

Dr. K. V. Suryabhagavan

Asst. Professor

School of Earth Sciences
Addis Ababa University

Acknowledgment

My first gratitude goes to the almighty GOD for the divine blessings and giving strength for me to complete this work.

I express my deep sense of gratitude and indebtedness to my advisor Dr. K. V. Suryabhagavan, Assistant Professor, School of Earth Sciences, Addis Ababa University, for his unlimited encouragements, helpful discussions and valuable suggestions.

I also wish to thank Dr. Seifu Kebede, Head, School of Earth Sciences, Addis Ababa University, for his permission to use the Remote Sensing Laboratory of the department of Earth science.

My gratitude also goes to the Ethiopian Water and Energy Office, Ethiopian National Meteorology Agency and Bahir Dar Meteorology Office for their deliver of required data and assistance during this work.

I am also grateful to Mr. Gebresilsie Welu, Head Department of Natural Resources Management, Wolaita Sodo University and to my colleagues who have assisted me financially and encouraging me during this research work.

My whole hearted thanks also go to all my friends, sisters and brothers whose names could not be mentioned separately, for their constant encouragement and cooperation.

Table of Contents

List of Figures

List of Tables

Abbreviations and symbols

u_*	Friction velocity in (ms^{-1})
BCM	billion cubic meter
C_p	air specific heat at constant pressure ($JKg^{-1}K^{-1}$) = 1004 J/kg
DN	Digital number
DOY	sequential Julian day of the year
dr	Earth-Sun distance in astronomical units
e_a	actual xivapour pressure
e_s	saturation vapour pressure
$ESUN_\lambda$	$ESUN_\lambda$ Mean solar exoatmospheric irradiances
ET_{24}	Daily evapotranspiration
ETrF or EF	evaporative fraction
G	Soil heat flux(W/m^{-2})
GCS	Geographic Coordinate System
G_{sc}	Solar constant
GW/Y	Giga watt per Year
h	Vegetation hieght
H	Sensible heat flux (W/m^{-2})
ITCZ	Inter-tropical Convergence Zone
k	Von Karmans constant (0.41)
K1	Calibration constant Kelvin $w/(m^{-2} * ster * \mu m)$
K2	Calibration constant Kelvin $w/(m^{-2} * ster * \mu m)$
L	Adjustment factor(0.5)
LAI	Leaf area Index
MAX	maximum

MIN	Minimum
NDVI	Normalised difference vegetation index
r_{ah}	Aerodynamic resistance to heat transport in(sm^{-1})
RL↓	Longwave incoming
RL↑	Longwave outgoing
R_n	Net Radiation
RS↓	Shortwave incoming
RS↑	Shortwave outgoing
SAVI	Soil adjusted vegetation Index
SEBAL	Surface Energy Balance algorithm for land
Ta	Air temperature
T_s	Surface temperature
WGS	World Geodetic System
z	elevation in meter
Z_{om}	Surface roughness for momentum transport
λ	Latent heat of vaporaization λ= $2.45*10^6$J/kg
μm	micrometer
ω_λ	weighted coefficient of the band
$\boldsymbol{\varepsilon}_{nb}$	Narrow band thermal emissivity (10.4 to 12.5 μm)
$\boldsymbol{\varepsilon}_o$	broad band thermal emissivity (6 to 14 μm)

Abstract

Lake Tana Basin which is found in Northwest highlands of Ethiopia has high potential for irrigation agriculture, hydroelectric power development and ecotourism. This basin has been identified as one of the economic growth corridors of the country and several hydropower and irrigation projects are being implemented. Hence, there is an increasing demand of water utilization and the water resource systems show variations in their accumulated flow, distribution and overall storage volume with time. The basic objective of this research was to estimate the daily and seasonal evapotranspiration of Tana basin and mapping its spatial distribution in different land use and land cover types. The Surface Energy Balance Algorithm for Land (SEBAL Model) was applied to three Landsat TM satellite images corresponding to November 18 and 27, 2011 to produce estimates of instantaneous actual evapotranspiration at 30×30m resolution for the satellite over pass time. Then, the instantaneous actual evapotranspiration was extrapolated to the daily ET value and seasonal accumulated ET values using the evaporative fraction which derived from the satellite images and the Penman Monteith reference evapotranspiration that was computed from meteorological data of the basin. The daily Penman-Monteith reference evapotranspiration ET_0 which calculated from meteorological data of the basin was found as 4.3 mm/day. The actual evapotranspiration of the basin computed using SEBAL model ranges from 0 to 4.3 mm/day that observed on bare lands and water bodies of the basin, respectively. The large portion of the basin has the range of evapotranspiration between 1.3 to 2.3 mm/day which covered by agricultural crops and grasslands. The dry season evapotranspiration of the basin also measured between 20 to 439 mm depth of water. The spatial distribution of evapotranspiration is related to the distribution of vegetation in the basin. The eastern and western parts of the basin show lower evapotranspiration corresponding to their little or no vegetation cover while the downstream of the Lake has relatively higher evapotranspiration due to its relatively dense vegetation cover. Finally, the daily SEBAL ET was compared to the Penman Monteith daily reference ET and the linear regression analysis shows that daily ET of the SEBAL model has a strong relationship with Penman-Monteith reference evapotranspiration of the study area.

Key Words: Evapotranspiration, Remote Sensing, Surface Energy Balance, SEBAL Model

CHAPTER 1 : INTRODUCTION

1.1. Background

Water is the most precious resource in all its forms (i.e. rainwater, aquifers, streams, lakes, rivers and water vapour). It plays a vital role in both environment and human life which provides a number of uses i.e. domestic uses, irrigation water for agriculture, hydroelectric power generation, transportation, tourism and recreation (Ateawung, 2010; Urama and Ozor, 2010).

Water is unevenly distributed resource both spatially and temporally on the Earth and some areas have plenty of water while others have shortage of water. The shortage of water is one of the main problems resulting from combined effects of climate change and increase in water demands for agricultural food production, urbanization and industries (IPCC, 1998*)*. The climate system has both direct and indirect impacts on the availability and spatial distribution of water resources and any changes in the climate system cause changes in the hydrologic system of a basin. Hence, the understanding of the natural water resource systems and the physical laws that govern the process of the hydrologic cycle has fundamental importance in the planning and implementation of water resource management strategies (Latha et al., 2010).

Water use has been growing twice more than the rate of population growth with 70% for irrigation agriculture, 22% for industry and 8% for domestic use (Blumenfeld et al., 2009). According to the UN Comprehensive Assessment of Fresh Water Resources of the World, about 31 countries are facing water stress and scarcity and over one billion people lack adequate access to clean drinking water (Barlow, 2001). The problem is more serious in Africa where the greater part of the population directly depends on agriculture as a source of livelihood and managing water resources has become more essential in the continent (Ateawung, 2010).

Ethiopia has high water resource potentials which called the ‘‘Water Towers of Northeast Africa’’ due to the existence of a number of perennial rivers which drains from highlands to lowlands and neighbouring countries (Alemayehu, 2006; McCornick et al., 2003). The country has twelve river basins with an annual flow volume of 122 billion m3 (BMC) of water and an estimated 2.6 up to 6.5 BMC of ground water potential (Azeze, 2014). Of these,

Abbay basin accounts the major part of irrigation and hydropower potential of the country. It has an irrigation potential of 815,581ha and a hydropower potential of 78,820 GWh/y (Awlachew et al., 2007). However, there is spatial and temporal scarcity of water for irrigation agriculture, domestic and municipal use due to lack of water storage infrastructure and high space and time variations in rainfall. Though the country has a substantial amount of water resources little has been developed for drinking water supply, hydropower, irrigation agriculture and other purposes and not generating the required amount of income from its available surface and ground water resources.

Sustainable management of water resources require detailed study of the hydrological elements such as precipitation, rate of infiltration, evapotranspiration, runoff and other parameters in relation to a specific basin or watershed. Of these, the precipitation, evapotranspiration and runoff are the principal components of water balance studies and information on these hydrological variables is useful for river basin hydrological studies, irrigation project planning and water rights regulation. Evapotranspiration can be measured using experimental weighing lysimeters directly on the field. However, these methods require high cost, time consuming and labour intensive and can only provide information on a specific location and the use of remotely sensed data from satellites provide an excellent means for determining and mapping the spatial and temporal structure of evapotranspiration from pixel to entire region (Oberg and Melesse, 2006).

The Surface Energy Balance Algorithm for Land (SEBAL Model), Surface Energy Balance System (SEBS) and the Soil Vegetation Atmosphere Transfer (SVAT Model) are some of evapotranspiration estimation models using the Surface Energy Balance method (Courault et al., 2005). The main purpose of this study is to characterize the spatial distribution of evapotranspiration of Lake Tana Basin in the north highlands of Ethiopia using Surface Energy Balance Algorithm for Land (SEBAL) model with Landsat satellite images and meteorological data of the study area.

1.2. Statement of the Problem

Water resources are limited in many parts of the world due to fast growing world population and impact of climate change that devastating to rivers, lakes, vegetation and ecosystems (Hassan et al., 2008). The changes in flow magnitude, variability and timing of the main flow events are among the most frequently cited hydrological issues. The impacts of climate change has adverse effects on water resource and other socio-economic developments of all nations and the problem is severe on developing countries like Ethiopia due to their nature dependent agriculture which is not capable of adjusting to such drastic changes (Taddele, 2009).

Lake Tana Basin is one of the major subbasins of the Abbay River Basin found in North westhighlands of Ethiopia. This basin has the biggest lake in Ethiopia (lake Tana) and it is characterized by plenty of natural resources (fauna and flora). However, the existing land and water resources system of the basin is adversely affected by the rapid growth of population, deforestation, surface erosion and sediment transport and the available land and water resources are not utilized effectively to improve the livelihood and socioeconomic conditions of the people (Setegne et al., 2008). In addition, Due to its high irrigation, hydropower generation, recreation and fishing potential there is an increasing demand for irrigation and hydropower development in Tana basin (Wale, 2008). Hence, this basin has been identified as one of the economic growth corridors of the country by the Federal Democratic Republic of Ethiopia and several hydropower and irrigation projects are being implemented and planned to implement in the basin (McCartney, 2010).

Despite of the enormous untapped potentials of the basin, the water resource systems show variations in their accumulated flow, distribution and overall storage volume with time and there is a need for research on the Tana Basin that can support improved catchment management programs and safeguarding the fast exploitation of the basin water resources. Several hydrological studies were conducted in the basin. However, they have their own limitations on spatial resolution and mapping the spatial distribution of the evapotranspiration of the basin. Therefore, this research was designed to estimate the evapotranspiration of the basin by using surface energy balance model (SEBAL model) from high resoulution (30m x30m) Landsat satellite images which has a significance role in understanding and mapping of the spatial distribution of evapotranspiration of Tana Basin.

1.3. Research Objectives

1.3.1. General Objectives

The main objective of this study was to determine the evapotranspiration rate of the basin through satellite remote sensing and geographic information system using the Surface Energy Balance Algorithm for Land (SEBAL Model).

1.3.2. Specific Objectives

The specific objectives of the research were to:

1. determine the reference evapotranspiration of the basin from meteorological data using Penman Monteith method,
2. determine the daily and seasonal evapotranspiration of the basin using SEBAL Model and
3. mapping the spatial distribution of evapotranspiration of the basin with the different land use types and land cover classes.

1.4. Research Questions

The main research questions of this research were:

1. How can satellite base remote sensing used to determine the actual and seasonal evapotranspiration in a basin scale?
2. What is the current evapotranspiration of the Lake Tana Basin and its spatial distribution over the different basin land use covers?
3. How can SEBAL Model used to determine evapotranspiration of the Lake Tana basin?

1.5. Significance of the Study

The sustainable use and planning of management strategies of water resources require well understanding of governing principles and gathering the available information. The determination of water resource system elements is essential part of water resources management. Both the surface and subsurface hydrological parameters such as precipitation, infiltration, percolation, ground water recharge, evapotranspiration, surface and subsurface runoff and other basin characteristic are valuable in hydrological and water balance studies and this research was conducted to determine the evapotranspiration of Lake Tana Basin from satellite remote sensing images using the Surface Energy Balance Algorithm for Land (SEBAL) model. Hence, it will use as a guide line for water balance studies, drought prediction and monitoring, water consumption rate and irrigation effectiveness in Lake Tana Basin and use as an indicator for ecological condition of the basin.

CHAPTER 2 : REVIEW OF LITERATURES

2.1. Global Water Budget and Hydrological Cycle

Water exists on the Earth with the three states of matter as solid ice crystals, liquid water and gaseous water vapour. The total amount of water on the earth is estimated about 1.4 x 10^9 km3. About 97.5% of this water is found in the oceans. Only about 2.5% is fresh water and out of this water, about 70% is frozen permanently in the polar ice caps and glaciers of the world (Shiklomanov, 1998). The remaining 30% is found in the lakes, reservoirs, rivers, and atmosphere and in the aquifers underground. The total fresh water available to human consumption and ecosystem is 0.27% of the global fresh water which accounts only 0.008% of the earth water budget (Blumenfeld et al., 2009).

Water circulates continuously between the oceans, land surface and atmosphere of the Earth (figure 2.1). The solar heat of the sun evaporates water form land and ocean surfaces and the vapour gets into the atmosphere. The uplifting of vapour to higher altitude causes the loss of its temperature (cooling) and forms precipitation that falls back to the Earth's surface. This continuous transfer and circulation of water between the Earth's surface and the atmosphere is known as *water cycle or hydrologic cycle* (Miralles, 2011).

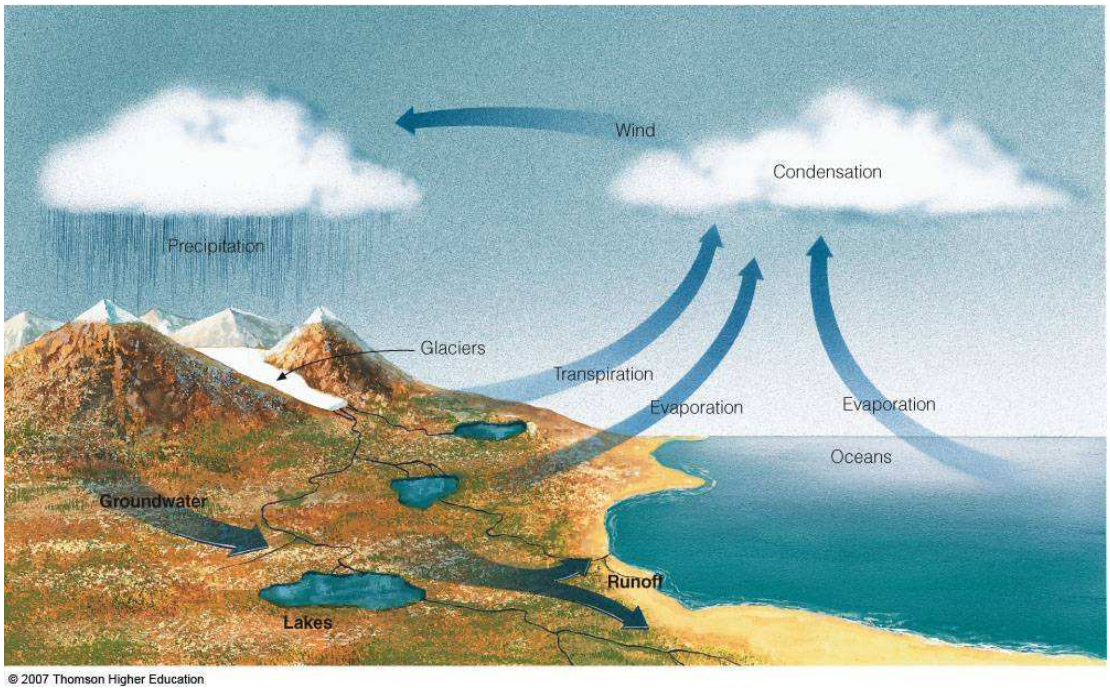

Figure 2.1. Hydrologic cycle

The global hydrological cycle involves different components such as precipitation, interception, infiltration, surface and subsurface runoff and evapotranspiration. Precipitation is the main source of water found in land surface, rivers, lakes and underground aquifers. Annually, about 458,000 km^3 of rain falls as atmospheric precipitation on the oceans and 119,000 km^3 on land surfaces. Similarly, evapotranspiration is an important and the second large component of the hydrological cycle next to precipitation (Iffendi, 2012). Every year about 577,000 km^3 water evaporates from the Earth surface which 502,800 km^3 from ocean and 74,200 km^3 from land surfaces. The difference between precipitation and evaporation from the land surface (44,800km^3/year) represents the total runoff of the Earth's rivers (42,700 km^3/year) and direct groundwater runoff to the ocean 2100 km^3/year. These are the principal sources of fresh water to support life on the Earth (Shiklomanov, 1998).

The hydrological cycle influences the variability of water resources and has a strong impact on every human life and ecological processes. The most significant parameters of the hydrologic cycle that control water availability in catchments are precipitation, evapotranspiration and surface & subsurface runoff. Of these, evapotranspiration and runoff respond largely to local climatic and land surface conditions, and have a strong local control on water balance since they reduce the total available water of a basin (Aduah et al., 2011). Therefore, detailed analysis and studies of the hydrologic system in river basin has a paramount importance for proper planning, development and implementation of water management strategies, climate modelling, hydrological and water balance studies.

2.2. Basic Concepts and Process of Evapotranspiration

Evapotranspiration refers to the combination of two separate processes whereby water is lost from the soil surface by evaporation and from the vegetation surface by transpiration. Evaporation and transpiration occur simultaneously and there is no easy way to distinguishing between the two processes. It is the physical process of conversion of water from its liquid state to the vapour state due to the available latent heat of vaporization (2.45 x 10^6J/kg). Evapotranspiration is the largest component in energy and hydrologic cycles that an average of about 50% of the absorbed solar energy and 60% of the total precipitation received to the Earth surface is lost to the atmosphere respectively (Miralles, 2011; Yan et al., 2012).

The rate of evapotranspiration from the evaporating surfaces such as water bodies, soil and plant surfaces depend up on the different climatic factors and the availability of moisture. Energy is required to change the state of the molecules of water from liquid to vapour. The direct solar radiation of the sun provide this latent heat of vaporization which is equvalent to 2.45 x 10^6J/kg. The driving force to remove water vapour from the evaporating surface is the difference between the water vapour pressure at the evaporating surface and that of the surrounding atmosphere. Hence, solar radiation, air temperature, air humidity and wind speed are the main climatological parameters that affect the evapotranspiration process. In addition, the vegetation characteristics, management practices and environmental aspects also affect the rate of evapotranspiration (Allen et al., 1998).

2.3. Types of Evapotranspiration

Evapotranspiration is the term used to express the loss of water from the surface to the atmosphere under different circumstances. Various physical and climatic parameters influence the rate of evapotranspiration, and the amount and available fraction of these parameters control the rate and process of evapotranspiration. Therefore, depending upon these conditions, evapotranspiration can be divided into three different classes and the following definitions explain the basic types of evapotranspiration (Weligepolage, 2005).

I. Reference Evapotranspiration

Reference Evapotranspiration (ETo) is the rate of water loss from a standard green grass (hypothetical surface) under the availability of adequate soil moisture. The reference surface represents extensive surface of green, well-watered grass of uniform height (15cm), actively growing and completely shading the ground. Since there is no shortage of soil moisture only the influence of climatic parameters considered and reference evapotranspiration is introduced to measure the evaporative demand of the atmosphere regardless of the crop type, crop development and management practices (Allen et al., 1998).

II. Potential Evapotranspiration

Potential Evapotranspiration (PET) is the maximum possible rate at which evapotranspiration would occur from a large area completely and uniformly covered with actively growing vegetation without the shortage of water under a given atmospheric condition.

III. Actual Evapotranspiration

Actual Evapotranspiration (AET) is the rate of evapotranspiration occurs under a given atmospheric condition and actual available soil moisture present within the soil. It can be directly derived from satellite images using surface energy balance models. In SEBAL model, instantaneous actual evapotranspiration can be computed using equation 3.33 for the satellite overpass time.

2.4. Methods of Estimating Evapotranspiration

The measurement of evapotranspiration is difficult in a field and it requires the accurate measurement of different physical and climatic parameters that control the rate of evapotranspiration (Miralles, 2011). Dalton was the first person attempts to estimate evaporation from atmospheric information in the beginning of 19^{th} century (1802). He points out the relationship of vapour pressure deficit (e_s - e_a) of the near surface air to the evaporation rate of water. Consequently, with understanding of the governing factors of evapotranspiration, several empirical equations were developed to estimate evapotranspiration depend on other climatic variables (Vinukollu et al., 2011).

According to Allen et al. (2006), Penman derived an equation to compute evaporation of open water surface from standard climatological records of sunshine, temperature, humidity and wind speed in 1948 by combining the energy balance equation and mass transfer method. His equation did not consider the land conditions affecting evaporation and the process is only based on the control of atmospheric factors. Hence, Penman's equation is not important to estimate evaporation of moisture limited areas. In 1964, Monteith developed a modified version of the Penman equation through introducing the surface and canopy resistance on the process of evapotranspiration and currently used as a well known Penman-Montieth combination equation. It remains the most accurate and physically based approach to estimate land surface evaporation. However, the main disadvantage of the method is its dependence on a large variety of observations that requires information on wind speed, surface roughness, available energy, vapour pressure and temperature.

currently, several evapotranspiration estimating methods (i.e. weighting lysimeter, eddy correlation system, Bowen ratio, scintillation and remote sensing) exist and those methods that have been currently applied for estimating evapotranspiration on global, regional and local scales can be classified into three main categories as (i) direct measurement methods,

(ii) hydrological or water balance methods and (iii) remote sensing methods or modeling the energy balance at the land surface (Iffendi, 2012; Kurkura, 2011).

2.4.1. Direct Measurement Methods

Direct measurement of evapotranspiration is very difficult and complex that requires specific instruments, site specific measurements and well trained personnel (Wang et al., 2011). The accurate measurement of various climatic and physical parameters or the soil water balance components are required to determine evapotranspiration. In practical applications, there is still no specific way to directly measure the actual ET over a watershed. Conventional ET estimation techniques such as pan-measurement, Bowen ratio, eddy correlation system, weighing lysimeter and scintillometer are considered as direct estimation methods of evapotranspiration which mainly based on site (field) measurements of physical parameters. These methods can provide relatively accurate estimates of ET over a homogeneous area, but have limited use since they are dependent on a number of physical and land parameters such as air temperature, wind speed, vapour pressure at a reference height, surface roughness etc, which are difficult to obtain over large scale terrain areas and difficult to be extrapolated or interpolated to various temporal and spatial scales with the required level of accuracy (Li et al., 2009).

Lysimeter

Lysimeters are devices or tanks filled with soil and buried in the ground to measure the direct loss of water from the soil and crop surfaces as evapotranspiration. This method involves growing of crops in the lysimeter installed in crop fields and measuring the water balance components (input and output of water i.e. precipitation, soil moisture storage and deep percolation) of the lysimeter (Weligepolage, 2005).

There are two main types of lysimeters, the drainage and the weighing types. In the first case, potential evapotranspiration is obtained as the difference between applied and drained water quantity. In the second case, changes in the total weight of the soil sample are measured and the actual evapotranspiration is determined by the changes in weight as water evaporates (Burnett, 2007). Lysimeters are the most accurate and direct measurement methods of estimating evapotranspiration. Therefore, they can be used as a standard measurement method for evaluating the performance of other physically based evapotranspiration models.

Eddy Covariance Method

Eddy covariance method is a micrometeorological technique that allows to measure directly the exchange of mass and energy (i.e. sensible heat, latent heat, H_2O vapour and other gases) between the atmosphere and underlying surface (Goulden et al., 1996). This approach considers the vertical movement of small parcels of air called eddies above a large homogeneous surface. In eddy covariance method, the fluctuations of vertical wind speed are correlated with fluctuations of water vapour density in atmosphere. The eddies transport water vapour and energy from the evaporating surface to the atmosphere, and can be used to estimate the amount of evapotranspirtion from the land or canopy surface to the atmosphere. The main disadvantages of these methods are often expensive, require accuracy of measurements and well trained research personnel (Wang et al., 2011). It can be calculated using the following equation (Brusaert, 1982).

$$ET = \rho_{\alpha} * \overline{w'q'} \quad \text{..... (2.1)}$$

where, E is evapotranspiration, w' is vertical wind speed and q' is specific humidity (kg of water per kg of air).

Bowen Ratio Method (β)

The eddy covariance technique is considered as the most accurate method to estimate the surface fluxes of sensible and latent heat. However, it requires high cost sensors and accurate measurements, and restricts its use to basic research studies (Adediji et al., 2007). Accordingly, it is common to use other methods like the Bowen ratio method to estimate these surface fluxes indirectly from temperature and humidity meteorological data.

Bowen assumed that the availability of both energy and moisture are the limiting factors of evapotranspiration and the transport mechanism of sensible heat and water vapour to the atmosphere are similar. Consequently, he derived the proportionality coefficient of sensible heat and latent heat fluxes by rearranging the energy balance equation. The Bowen ratio is expressed as (Perez et al., 1999).

$$\beta = H/\lambda E \quad \text{..... (2.2)}$$

where, β is Bowen ration, H is sensible heat flux (W/m^2), λE is latent heat flux (W/m^2). Then, by rearranging the above equation (Verma et al., 1978).

$$\beta = \gamma * \left(\frac{T_s - T_a}{e_s - e_a}\right) \quad \text{..... (2.3)}$$

where, β is Bowen ration, γ is psychometric constant, T_s and T_a are the surface and air temperature , e_s and e_a are the saturation and actual vapour pressures respectively.

2.4.2. Water Balance Methods

The water balance study of a lake, watershed or reservoir has a great role to understand the hydrologic processes taking place in the water body and it helps to plan & implement the required development and management activities. This method involves the estimation of all the water inflow and outflow components of a lake, watershed or water reservoir for a given period of time (Mulushewa, 2013). The water balance method involves applying the water balance equation to the catchment area of interest over a time period ΔT and solving the equation for evapotranspiration as (Kurkura, 2011).

$ET = P + Q_{in} + G_{in} - Q_{out} - G_{out} - \Delta S$ ..... (2.4)

where, ET is evapotranspiration, P is precipitation, Q_{in} is surface inflow water, Q_{out} is surface outflow water, G_{in} is inflow ground water, G_{out} is outflow ground water and ΔS is change in stored water over the time period.

2.5. Remote Sensing Methods

Remote Sensing (RS) is defined as the science of acquiring information about an object, area or phenomena through the analysis of data obtained by a device (sensors) that is not in physical contact with the target object under investigation. Target objects in remote sensing images may be any feature, object or phenomena which can be observed and distinguished from other features in the image (Bakker et al., 2000).

2.5.1. Basic Principles of Remote Sensing

Remote sensing of the earth surface involves sensing and recording of the reflected or emitted energy (electromagnetic radiation) from the surface of the target object, and processing & analysing it as a source of information. All objects with surface temperature above absolute zero (0^0k, -273^0c) radiate electromagnetic energy due to molecular agitation, and regardless of the black body, when electromagnetic radiation strikes their surface all objects of the earth's surface have their own spectral reflectance nature that can be used in remote sensing

to distinguish one object or event from the other. Therefore, remotely sensed images record the interaction of electromagnetic energy with the earth's surface (Harvey, 2008; Reddy, 2008).

Remotely sensed data can be collected using devices like sensors, films, digital cameras and video recorders from a various platforms such as satellites, aircrafts, vehicles and handheld radiometers. Sensors that can be used to measure electromagnetic radiation are classified as passive and active sensors. Sensors without their own source of radiation and only which are sensitive to radiation from a natural source are passive sensors (i.e. satellite sensors) and sensors with their own energy source or flash are active sensors. The most familiar example of active remote sensing is RADAR (Radio Detection and Ranging) that emits its own energy in the microwave region of electromagnetic spectrum. Remote sensors are designed to measure energy in wide ranges of electromagnetic spectrum i.e. short wave, visible light, infrared and thermal bands (Kurkura, 2011).

Remotely sensed data can be represented either in analogue or digital format. Images displayed in a pictorial or photograph type are in analogue format, but images represented in computer arrays of digital numbers corresponding to a pixel that representing the brightness level of that pixel in the image are in digital format.

2.5.2. History of Remote Sensing

Remote sensing of the earth surface has a long history dating to the first discovery of a photograph image by Niepce and Daguerre in 1839. The photographic camera became the first practical remote sensing device around 1850. In early 1859, photographs taken from balloons and pigeons were used for military applications and following the invention of the aircraft in 1903, aerial photography were used on a large scale for photo reconnaissance during World War first in Europe. It was the first method of remote sensing and even used today in the era of satellite and electronic scanners. Aerial photography remains still the most widely used type of remote sensing (Konecny, 2003; Schowengerdt, 2007).

The period from 1960 to 1980 has experienced some major changes in the field of remote sensing. Among these, the term remote sensing is first used instead of aerial photography in 1960, sensor platforms has changed from air planes to satellites and remotely sensed analog data has changed to digital data format due to the advancement and availability of small

micro-computers to display and analyze satellite imageries (Baumann, 2009). The first meteorological satellite called TIROS was lounched in 1960. The first remote sensing satellite, Earth Resources Technology Satellite (ERTS-1) later called Landsat 1 lounched in 1972 by NASA, the National Aeronautics and Space Administration of the United States with a spatial resolution of 80m pixels in four spectral visible and near infrared channels. In subsequent years both spatial and spectral resolution of the first Landsat were improved and Landsat 3 launched in 1982 with six visible and near infrared channels at 30m pixels and one thermal channel at 120m pixels. Higher spatial resolution was achieved by the French Spot satellites launched since 1986 with panchromatic pixel sizes of 10m and multispectral resolution at 20m pixels (Konecny, 2003). Consquently, many countries including Canada, India, Israel, Japan, South Korea and Taiwan, and multinational agencies such as the European Space Agency (ESA) now operate remote sensing systems (Schowengerdt, 2007).

2.5.3. Application of GIS and Remote Sensing for Natural Resource Mapping

Remote Sensing technology has highly significant capabilities to provide information on natural resources such as crop, land use, soils, forest etc on regular basis. Similarly, Geographic Information Systems (GIS) are the latest tools available to store, retrieve and analyze different types of data for management of natural resources. GIS facilitates systematic handling of data to generate information in a devised format. Thus, it plays an important role in evolving alternate scenarios for natural resources management.

RS data and GIS play a rapidly increasing role in the field of hydrology and water resources development. Although very few remotely sensed data can be directly applied in hydrology, such information is of great value since many hydrological relevant data can be derived from remote sensing information. One of the greatest advantages of using RS data for hydrological modelling and monitoring is its ability to generate information in spatial and temporal domain, which is very crucial for successful model analysis, prediction and validation. However, the use of RS technology involves large amount of spatial data management and requires an efficient system to handle such data. The GIS technology provides suitable alternatives for efficient management of large and complex databases.

Image data have been used as a primary source of natural resources information in thematic mapping, which in turn is utilized in various hydrological studies (Seth et al., 1996). The

remote sensing data provides synoptic view of a large area in the narrow and discrete bands of the electromagnetic spectrum at regular intervals. The space borne multispectral data enable generating timely, reliable and cost effective information on various natural resources, namely surface water, ground water, land use/cover, soil, forest cover and environmental hazards, namely water logging, salinity and alkalinity, soil erosion by water etc.

2.5.4. Remote Sensing Models to Estimate Evapotranspiration

Evapotranspiration is the most important component in both global energy and water budgets of the Earth. It requires relatively large amounts of energy in the form of latent heat or radiant energy. Hence, the process of evapotranspiration is governed by the exchange of energy at the land and vegetation surface and it is limited by the amount of energy available. Since evapotranspiration is the single parameter that links global energy and water budgets of the earth, it is possible to predict the regional actual evapotranspiration by applying the principle of energy conservation (Weligepolage, 2005).

Among the several ET estimation methods, remote sensing is one of the most reliable methods of estimating actual evapotranspiration based on surface energy balance equation. It provides the possibilities to quantify surface energy fluxes from consistent recording and analysis of spectral reflectance and emittance of radiation over a large surface. The use of remote sensing is the recent development to resolve the challenge of the spatial distribution of evapotranspiration. Its capability of observing a number of physical characteristics of the earth's surface has been found useful for the parameterization of models for regional ET estimation using remote sensing technique (Kurkura, 2011).

Remote Sensing approach can provide more efficient and economically feasible outputs with relatively high spatial and temporal resolution than point measurements for evaluation of both surface and atmospheric processes including evapotranspiration (Almhab, 2009; Burnett, 2007; Li et al., 2009).

2.6. Previous Studies on the Study Area

This section presents a general review of hydrological and water balance studies conducted in Lake Tana basin to characterize its hydrology and environment. As reviewed in different literatures, several studies were conducted in Lake Tana basin by different researchers and scientists. Those earlier bathymetric surveys of Lake Tana and the recently conducted hydrological and water balance studies provide brief description and help to understand the hydrological characteristics of the basin. Some of these are Melkamu (2005) 1655mm/year, Kebede et al. (2006) 1478 mm/year, Yohannes (2007) 1666mm/year, SMEC (2008) 1675mm/year and Abeyou (2008) 1690 mm/year. However, most of these researches are conducted by using the hydrological models and water balance method of the basin. The above studies are mainly characterized by the estimation of water balance of the basin from flow gauging stations and simulation of the ungauged catchments by analysis of meteorological data. In these approaches, data used from both gauging and ungauged catchments has its own limitation to show the spatial distribution of the hydrological variables over the surface area of the basin.

The evapotranspiration and water balance of Lake Tana Basin was studied by Pelgrum and Bastiaanssen (2006) by means of advanced remote sensing technologies. The surface energy balance algorithm for land (SEBAL model) was used to map the spatial distribution of evapotranspiration of the Tana Beles sub-basins from the MODIS (Moderate Resolution Imaging Spectroradiometer) satellite image which is about 250m x250m pixel resolution. According to Molla (2009) Landsat satellites with high spatial ground resolution (e.g. 30 m × 30 m) can provide more accurate shape and spectral characteristics of the ground objects as a result of their relatively small pixel size than those of MODIS or the NOAA (AVHRR) satellites which have pixels of 1000 m × 1000 m and 1100 m × 1100 m, respectively. As a result, the study of evapotranspiration of Lake Tana basin by using the surface energy balance model (i.e. SEBAL model) from high resolution Landsat satellite images is the other relatively accurate estimation of evapotranspiration with its spatial distribution.

CHAPTER 3 : MATERIALS AND METHODS

3.1. Description of the Study Area

Lake Tana basin is the source of the Blue Nile River and located in the north-west highlands of Ethiopia. It has a total drainage area of approximately 15,000 km^2 (Figure 3.1) including the lake area of 3,156 km^2 and an altitude of 1,786m above mean sea level. The basin extends with length of 200km north to south and width of 165km east to west. It lies between 10.95^o and 12.78^{0}N latitude and 36.89^o and 38.25^{o}E longitude.

Lake Tana is the largest lake in Ethiopia and the third largest in Nile Basin. It is approximately 84km long and 66km wide which is located in the north-west highlands of 11.62^0 to 12.31^{0}N latitude and 37.01^0 to 37.64^{0}E longitude and 564 kms away from Addis Ababa. The lake is a natural freshwater with a mean and maximum depth of 9m and 14m respectively.

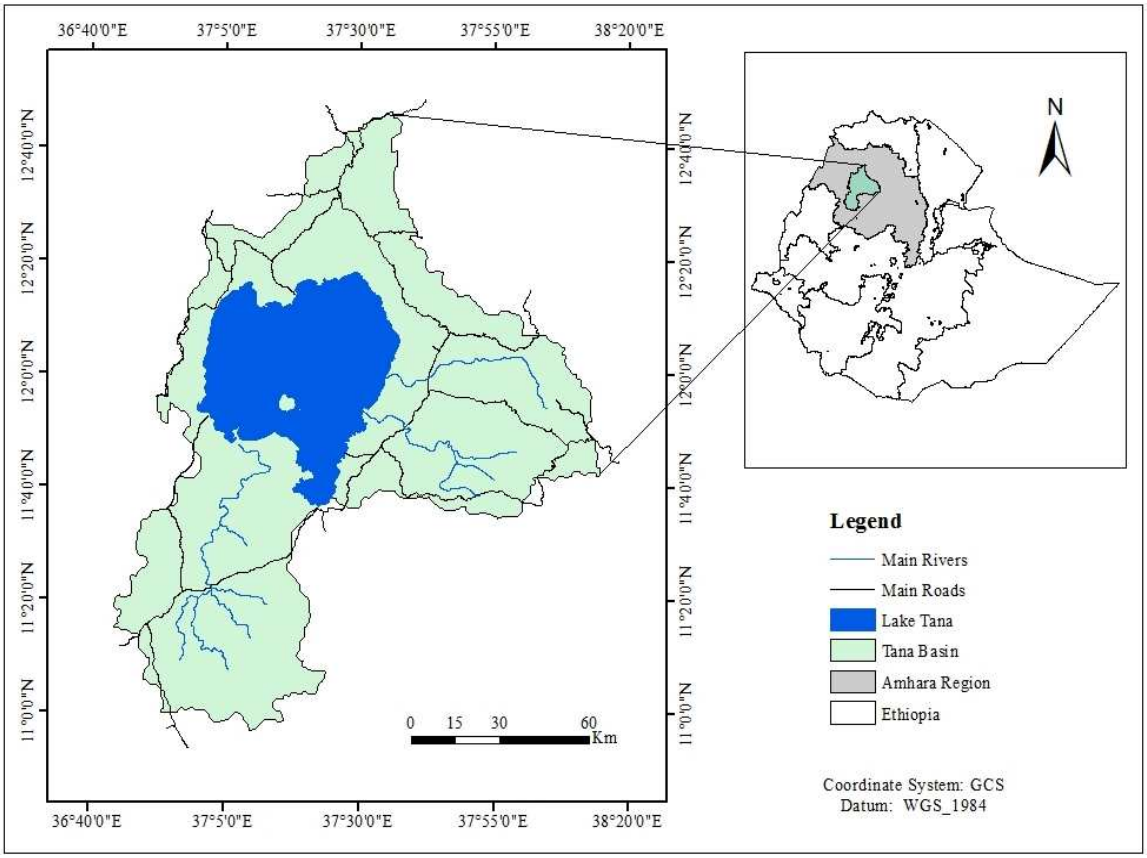

Figure 3.1. Location map of the study area

3.2. Climatic Condition of Lake Tana Basin

The climate of Ethiopia is mainly controlled by the topographic nature of the country and the seasonal movement of the Inter-tropical Convergence Zone (ITCZ) rather than its latitudinal location. The extreme high elevation difference between the highland and lowland areas of Ethiopia makes diversified climatic regions of the country. The climatic condition of the country is ranging semi-arid desert type in the lowland rift valley and humid type in the southwest parts to mountain highlands of the country (Kebede et al., 2006; Wale, 2008).

The climate of Lake Tana basin is dominated by tropical highland monsoon climate type mainly with three recognized seasons. First, the summer season (kremt) exists generally from June to September during which south-west wet winds bring moisture from the Atlantic and Indian oceans. The maximum amount of rainfall (80%) is received during this season. Second, the dry season (Bega) lasts from October to January during which the north-east Himalayan dry winds flow towards the Atlantic and Indian oceans which are associated with clear skies, maximum sunshine, high daily temperature variation, and low relative humidity. Third, the minor rainy season (Belg) lasts from February to May during which south-east wet winds bring the small amount of moisture from the Atlantic and Indian oceans. The climatic condition of Lake Tana Basin also shows high variability both in space and time within the basin. The southern part of the basin is characterised by high rain fall while the upper northern part of the basin receives relatively lower amount of rainfall.

3.2.1. Temperature and Rainfall

Lake Tana Basin has relatively uniform temperature throught the year with slight incease during march, april and may as shown in table 3.1. However, it has high diurnal difference. The annual average daily maximum and minimum temprateure at Bahir Dar station are 27.7^0c and 13.12^0c respectively. Table 3.2 shows the mean annual temperature of Tana Basin from 2003 to 2012 years.

Table 3.1. Mean monthly temperature of Tana Basin (2003-2012)

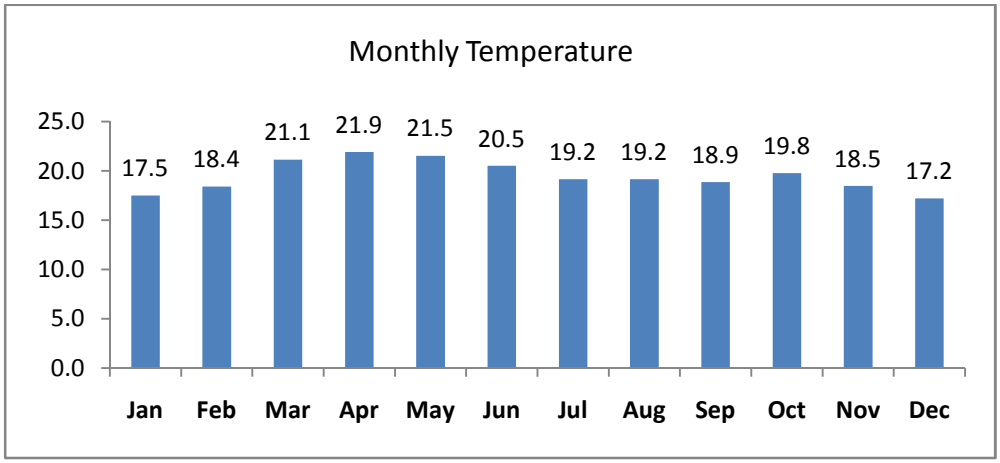

Table 3.2. Mean annual temperature of Tana Basin (2003-2012)

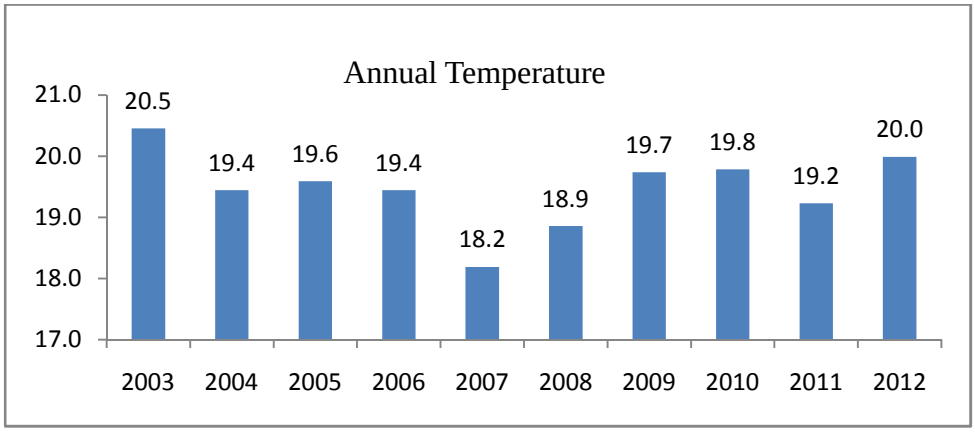

The annual rainfall of Lake Tana Basin ranges between 1191.9 to 1525.8 mm with an average of 1352.24 mm at Bahir Dar station as shown in table 3.3 and 978.1 to 1238.9 mm with an average of 1108.5 mm at Gondar. Rainfall shows variation in space and time within the basin. The southern part of Tana basin relatively receives high rainfall than the north part of the basin.

Table 3.3. Annual rainfall of Tana Basin (2003-2012)

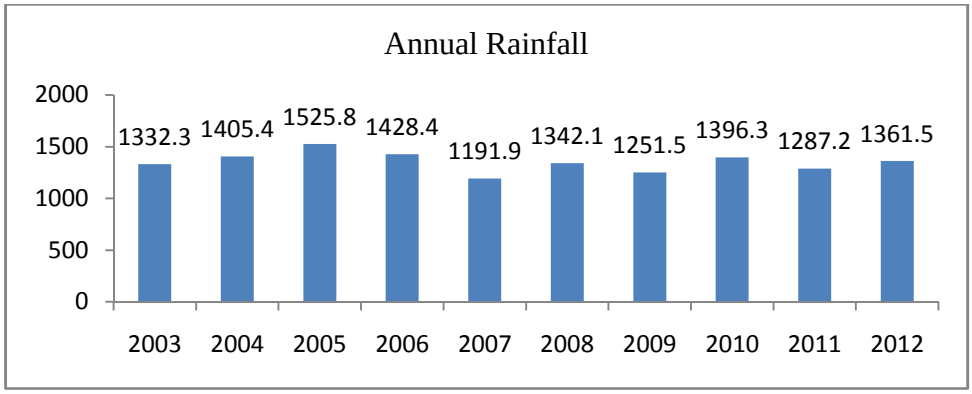

3.3. Topography and Soils

The Lake Tana basin is characterized by a large flat area to very gently sloping plain bordering the lake on the north and east and an extensive area of rolling to hilly uplands on the south with 1672 m and 4090 m minimum and maximum elevations respectively. Figure 3.2 shows the elevation characterstics of Tana Basin.

Soils in most of the Tana Basin are derived from the weathered basalt profiles and are highly variable. In low lying areas particularly north and east of Lake Tana and along parts of Gilgel Abay, soil have been developed on alluvial sediments. The major soil types in the area includes chromic luvisols, eutric cambisols, eutric fluvisols, eutric leptosols, eutric regosols,, eutric vertisols, haplic luvisols, haplic alisols, haplic nitisols, and lithic leptosols (Dile, 2009).

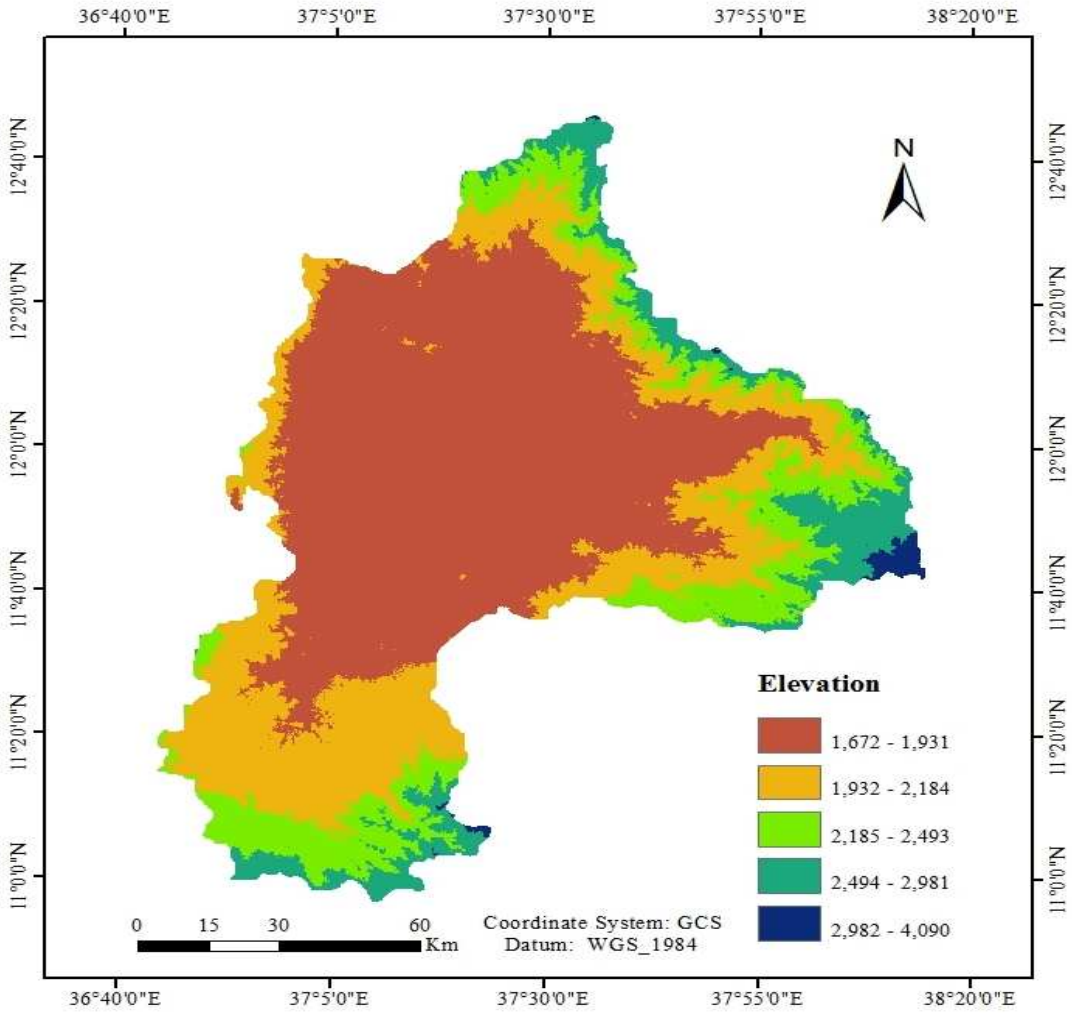

Figure 3.2. Digital elevation model of Tana Basin

3.4. Drainage System of Tana Basin

About 40 seasonal and perennial rivers feed the lake and Gilgel Abbay, Gumera, Ribb and Megech Rivers are the main inflows of Lake Tana. According to Kebede et al. (2006) those four rivers contribute 93% of the lake inflow. The water level of the lake rises gradually during the rainy season to reach its maximum level in September at the end of the rainy season and after which it slowly falls to reach its minimum water level in June. The only river flowing out of Lake Tana is the Abbay River that contributes 7% of the Blue Nile River water. Figure 3.3 shows the drainage system of Tana Basin.

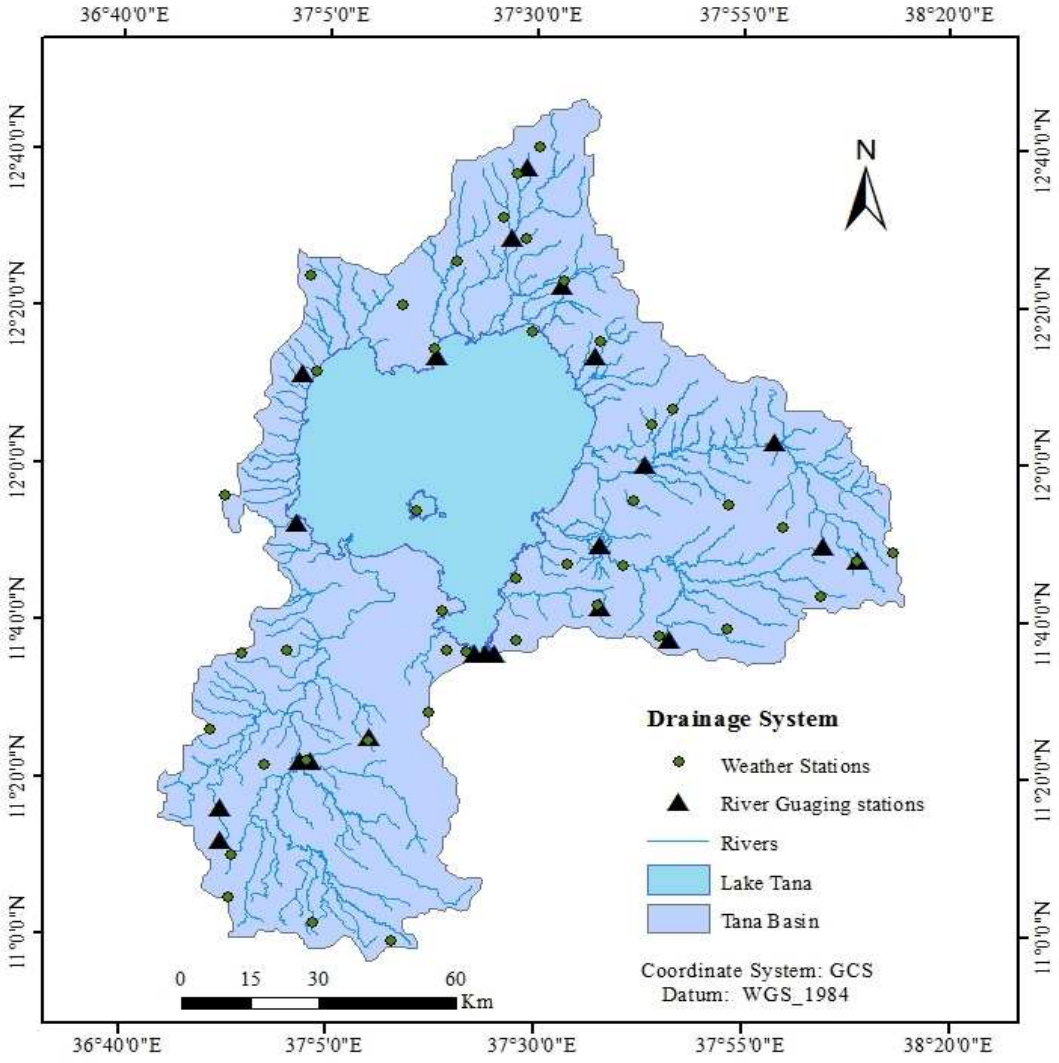

Figure 3.3. Drainage system of Tana Basin

3.5. Data Sources and Collection Methods

In this research, both remote sensing and ground based data were collected for estimation of evapotranspiration of Tana Basin using SEBAL model. The remote sensing data includes satellite images, digital elevation model and image header files.

3.5.1. Remote Sensing Data

The Landsat satellite images of the basin and 30m x 30m Digital Elevation Model were collected to map evapotranspiration of Tana basin. The basin lies on three Landsat satellite images of 170/051 and 170/052 and 169/052 path and rows, respectively. Table 3.4 shows the Landsat satellite images which used for mapping the daily and seasonal evapotranspiration of Tana basin.

Table 3.4. Remote sensing data characteristics

No	Path and Row	Type of sensor	Acquision date
1	169/052	TM Landsat 5	27/11/2011
2	170/051	TM Landsat 5	18/11/2011
3	170/052	TM Landsat 5	18/11/2011

3.5.2. Meteorological Data

For the determination of evapotranspiration of the basin by satellite remote sensing, both the raw and daily weather data of the area such as minimum and maximum temperature, wind speed at two meter height, humidity, length of sunshine hours and rain fall data were collected from the Ethiopian National Meteorological Agency.

3.5.3. Ground Field Survey Data

Satellite based GPS provides accurate geo-referenced positional locations and boundaries. It has different applications such as land use land cover mapping, effective navigation for a particular site, transportation and communication. GPS based field observation and post verification is conducted to check the information on satellite images to the ground actual information.

3.6. Methods of Data Pre-processing and Analysis

Remote sensing data are available in digital format and digital image processing is a technique to improve the quality of an image for different application. Satellite image pre-processing operations are those operations done on the image before the analysis and interpretation process begins to increase the accuracy of information that can be extracted from the satellite image (Lillesand and Kiefer, 2000). According to Moulich and Ghosha (2013) all satellite image processing operations can be grouped into three categories: Image Rectification and Restoration, Enhancement and Information Extraction.

3.6.1. Geometric and Radiometric Corrections

Raw digital image cannot be used without geometric and radiometric correction. The process of both geometrical and radiometric corrections of raw digital images is known as rectification. Raw digital images can be corrected with either corrected image or georeferenced topographic map of the same area by collecting ground control points (GCPs), which are clearly identifiable features such as road connection, river connection and other permanent features on both correct image and distorted image (Lillesand and Kiefer, 2004). For this study, the raw satellite images were orthorecitified in projected coordinate system with the image source company using nearest neighbourhood resampling technique and image coordinate transformation was done to geographic coordinate system.

Radiometric distortion is caused by scene illumination, atmospheric conditions (include absorptions, scattering, emissions) and instrument response characteristics and it is difficult to avoid the noise but it has been reduced the effect from the raw data. SEBAL model is more appropriate and gives good result in relatively stable atmospheric conditions. Hence, satellite images were pre-processed before the final application for the model and appropriate atmospheric corrections such as masking cloud covers were applied to the satellite images.

3.6.2. Image Enhancement

Image Enhancement procedures were performed for the image to improve visual interpretability of the image by increasing clear contrast among various features view. These operations was completed in ERDAS imagine software specifically by nose removal techniques. Contrast stretching and spatial filtering are some good examples of image

enhancement where contrast stretching increases the tonal distinction among various features in a scene and spatial filtering enhances specific spatial patterns in an image.

3.6.3. Research Methodology

The general methodology of the study is schematically described in Figure 3.4 as a step by step SEBAL processing procedure.

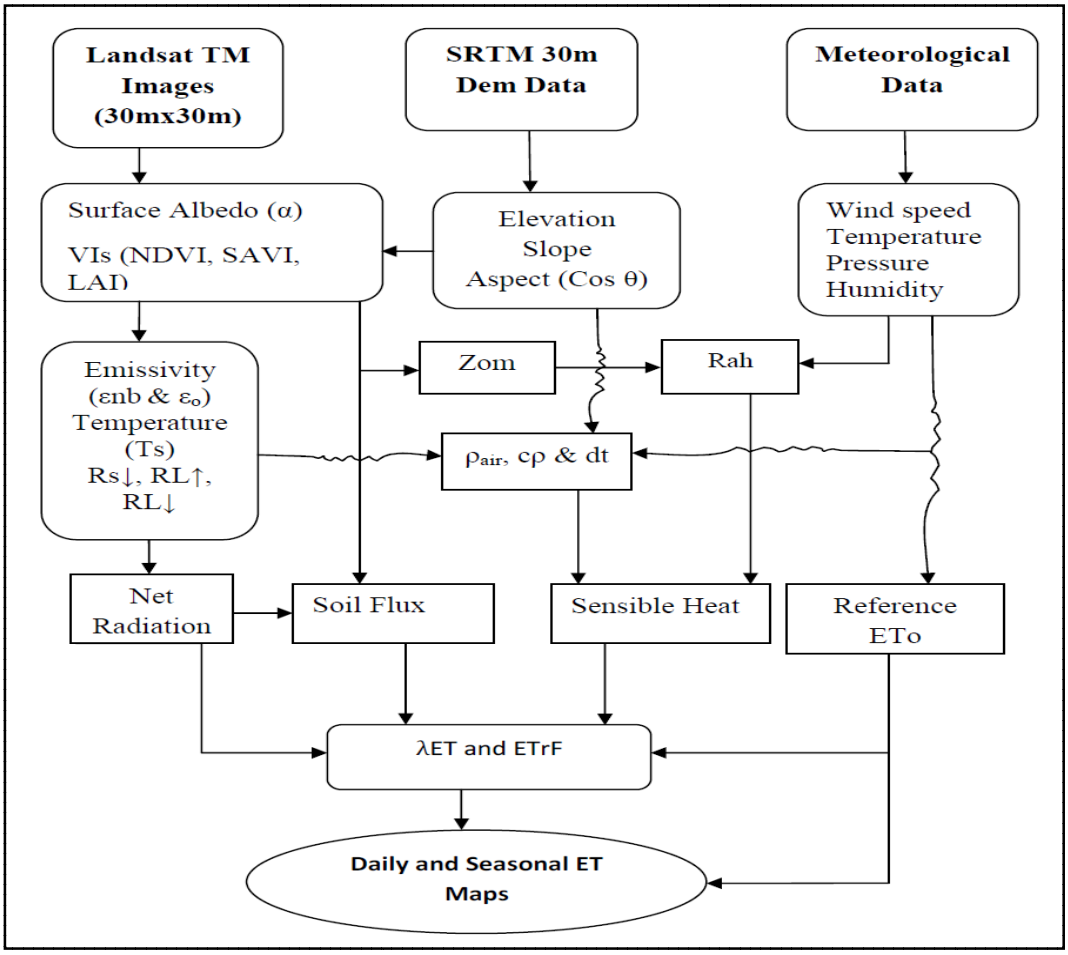

Figure 3.4. General flow chart of research methodology

3.7. Basic Principles and Procedures of SEBAL Model

SEBAL Model which stands for the Surface Energy Balance Algorithm for Land is the characterization and quantification of the surface energy fluxes based on the spectral satellite measurements. It is an image-processing model that calculates the actual ET and other energy exchanges between land and atmosphere (Bastiaansssen et al., 1998a; 2000). SEBAL calculates evapotranspiration in a series of computations that generate surface flux parameters such as net radiation, soil heat flux and sensible heat flux to the air. This model

computes a complete radiation and energy balance along with the resistances for momentum, heat and water vapour transport for every individual pixel. The resistances are a function of state conditions such as level of soil moisture, wind speed and air temperature.

In SEBAL model, evapotranspiration can be computed from satellite images and weather data using the surface energy balance. It requires weather data parameters such as wind speed, humidity, solar radiation and air temperature of the area of interest. A land use map for the area of interest is also helpful. SEBAL uses the visible, near infrared and thermal spectral input data from the multispectral satellite imageries and computes the instantaneous evapotranspiration flux for the satellite over pass time as the residual energy flux of the surface energy budget equation (Giridhar and Suneel, 2014).

$$Rn = G + H + \lambda ET \quad \text{..... (3.1)}$$

Where, R_n is the net radiation flux at the surface (W/m^2), G is the soil heat flux (W/m^2), H is the sensible heat flux to the air (W/m^2) and λET is the latent heat flux (W/m^2).

In the above equation, the soil heat and sensible heat fluxes are subtracted from the net radiant flux at the surface to compute the residual energy available for evapotranspiration (λET). Soil heat flux is empirically computed using vegetation indices, surface temperature and surface albedo. Sensible heat flux is computed using the wind speed observation, estimated surface roughness and surface to air temperature differences. SEBAL uses an iterative process to correct for atmospheric instability due to the buoyancy effects of surface heating (Giridhar and Suneel, 2014).

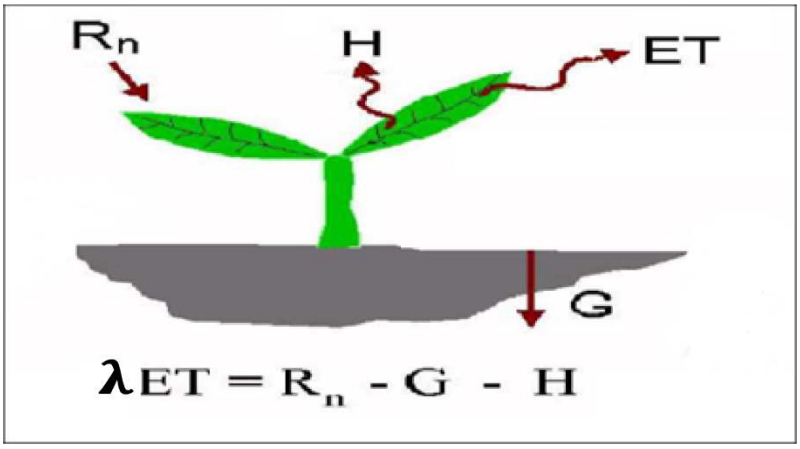

Figure 3.5. Surface energy balance

In remote sensing estimation of evapotranspiration, first the satellite radiance converts into land surface characteristics such as surface albedo, leaf area index, vegetation index and surface temperature. Then, indiviual surface energy fluxes such as the net radiation, soil haet flux, sensible heat flux and the avialable latent heat that evaporates water from the surface are computed using the ERDAS model builder. Finaly, instantaneous evapotranspiration is computed which is extrapolated to daily and longer periods. A comprehensive description of SEBAL is available from Bastiaansssen et al. (1998a; 1998b).

3.7.1. Conversion of DN to Spectral Radiance

The spectral radiance of the band is the amount of outgoing radiation energy of the band detected at the top of the atmosphere by the satellite. The satellite sensor captures the heat energy units come from the surface and store this information as a digital number (DN) with the range of 0 to 255. The DN values of each band converted to the spectral radiance units before the computation of the reflectivity of each band. It can be calculated using the following equation.

$$L\lambda = \left(\frac{Lmax - Lmin}{Qcalmax - Qcalmin}\right) * (DN - Qcalmin) + Lmin \quad \text{..... (3.2)}$$

Where; DN is the digital number of each pixel, LMAX and LMIN are calibration constants of each band as shown in table 3.5, QCALMAX and QCALMIN are the highest and lowest range of values for rescaled radiance in DN. The units for L_λ are $W/m^2/sr/\mu m$. For the NLPS generating system, the QCALMIN is 0 and for the LPGS generating system, the QCALMIN is 1. The values of the LMAX, LMIN, QCALMAX and QCALMIN of each band can be found from the satellite image header file.

Table 3.5. LMAX and LMIN of Landsat 5 TM satellite (image header file)

	Band 1	Band 2	Band 3	Band 4	Band 5	Band 6	Band 7
LMIN	-1.52	-2.84	-1.17	-1.51	-0.37	1.238	-0.15
LMAX	193	365	264	221	30.2	15.303	16.5

3.7.2. Reflectivity of Bands at the Top of Atmosphere

The reflectivity of an object is defined as the ratio of the reflected radiation flux to the incident radiation flux. The reflectivity of each band (ρλ) is the ratio of reflected radiation

flux to the incident radiation flux measured at the top of the atmosphere by the satellite sensor (for a single band) and it describes the combined earth-atmosphere behaviour with respect to the reflected solar radiation. It is computed using the following equation.

$$\rho\lambda = \frac{\pi * L\lambda}{ESUN\lambda * COS\theta * dr} \quad \text{..... (3.3)}$$

Where, L_λ is the spectral radiance for each band, $ESUN_\lambda$ is the mean solar exo-atmospheric irradiance for each band ($W/m^2/\mu m$), cos θ is the cosine of the solar incidence angle (from nadir), and d_r is the inverse squared relative Earth-sun distance. The cosine θ is computed using the sun elevation angle (β) where $\theta = (90^0 - \beta)$ for the flat areas.

The d_r is the relative distance between the earth and the sun in astronomical units. It is computed using the following equation (Allen et al., 1998).

$$dr = 1 + 0.033Cos\theta(DOY * \frac{2\pi}{365}) \quad \text{..... (3.4)}$$

Where, DOY is the sequential Julian day of the year and the angle (DOY * 2π/365) is in radians. Values for d_r range from 0.97 to 1.03 and are dimensionless.

Table 3.6. ESUN**λ** for Landsat 5 TM satellite

Sensor	Band 1	Band 2	Band 3	Band 4	Band 5	Band 6	Band 7
TM 5	1957	1829	1557	1047	219.3	-	74.52

The combined albedo for all bands at the top of the atmosphere (α_{top}) which is not adjusted for the transmissivity of the atmosphere also calculated from the reflectivity of each band at the top of the atmosphere and their corresponding weighted coefficient using the following equation.

$$\alpha_{top} = \sum_{i=1}^{n}(\omega_{\lambda i} * \rho_{\lambda i}) \quad \text{..... (3.5)}$$

Where, α_{top} is the albedo at the top of the atmosphere, $\omega_{\lambda i}$ is the weighted coefficient of band one and $\rho_{\lambda i}$ is the reflectivity of band one.

Table 3.7. Weighting coefficients of Landsat 5 TM satellite

Sensor	Band 1	Band 2	Band 3	Band 4	Band 5	Band 6	Band 7
TM 5	0.293	0.274	0.233	0.157	0.033	-	0.011

3.7.3. Surface Albedo

Surface albedo is the ratio of reflected solar radiation to the incident solar radiation at the ground surface of the Earth. It is a non-dimensional and unitless quantity that indicates how a surface reflects solar energy. Surface albedo ranges between 0 and 1 at which 0 meaning a black object that absorbs all the incoming energy and 1 meaning a white object that reflects all incoming energy. The surface albedo is computed from the albedo of top atmosphere (α_{top}) that derived from the reflectivity of each band, path-radiance and transmissivity of the atmosphere using equation 3.6. Figure 3.5 shows the surface albedo of Tana Basin which ranges from 0.32 to 0.45.

$$\alpha = \frac{\alpha_{top} - \alpha_{path\_radiance}}{\tau_{sw}^2} \quad \text{..... (3.6)}$$

Where; $\alpha_{path\ radiance}$ is the average portion of the incoming solar radiation across all bands that is back-scattered to the satellite before it reaches the earth's surface, and τ_{sw} is the atmospheric transmissivity.

The values for $\alpha_{path\ radiance}$ range between 0.025 and 0.04 and for SEBAL a value of 0.03 is recommended based on Bastiaanssen (2000). Atmospheric transmissivity is defined as the fraction of incident radiation that is transmitted by the atmosphere and it represents the effects of absorption and reflection occurring within the atmosphere. This effect occurs to incoming radiation and to outgoing radiation and τ_{sw} includes transmissivity of both direct solar beam radiation and diffuses (scattered) radiation to the surface. Assuming clear sky and relatively dry conditions using an elevation-based relationship (FAO, 2006), it can be computed as:

$$\tau_{sw} = 0.75 + 2 * 10^{-5} * z \quad \text{.....(3.7)}$$

Where; z is the elevation above sea level (m) and represents the elevation of the weather station.

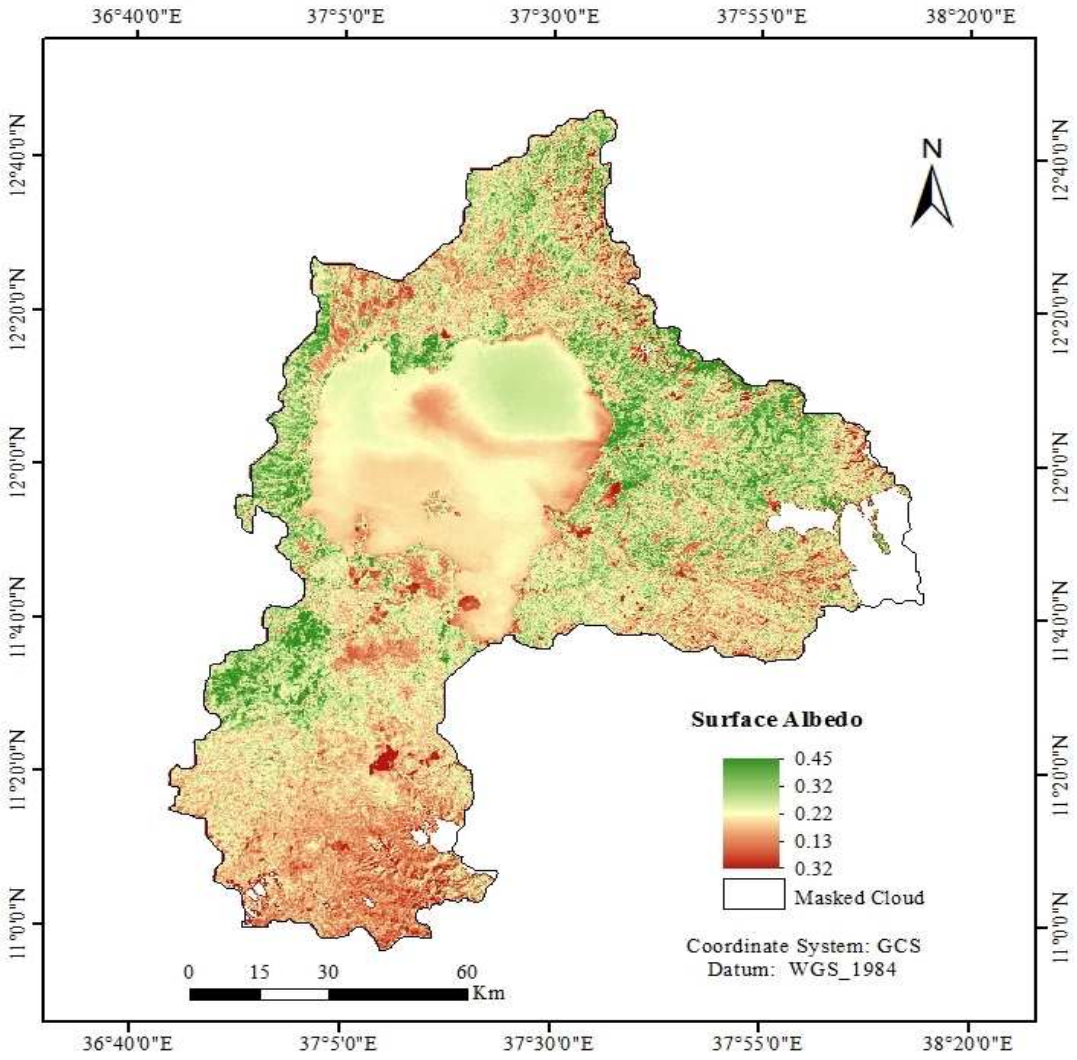

Figure 3.6. Surface albedo

3.7.4. Incoming Shortwave Radiation

A relatively constant amount of solar radiation reaches to the horizontal outer surface of the atmosphere with average distance between the sun and the earth. This radiation possesses different process such as absorbed, reflected and diffused by the atmospheric particles and finally reaches to the earth surface. This direct and diffuse solar radiation flux that actually reaches to the earth surface is the incoming shortwave radiation (w/m^2). The incoming shortwave radiation ($R_{S\downarrow}$) is computed using the solar constant, the solar incidence angle, a relative earth-sun distance, and a computed atmospheric transmissivity. By assuming a clear sky conditions for the imaging time, it can be calculated as:

$Rs\downarrow = Gsc * \cos\theta * dr * \tau_{sw}$ …… (3.8)

Where, G_{sc} is the solar constant (1367 W/m^2), cos θ is the cosine of the solar incidence angle, d_r is the inverse squared relative earth-sun distance, and τ_{sw} is the atmospheric transmissivity.

3.7.5. Biophysical Parameters

The biophysical parameters derived from the near infrared band and red band reflectance's that provide information to characterise the vegetation and land cover status of the surface. These three major vegetation indices are the Normalized Difference Vegetation Index (NDVI), the Soil Adjusted vegetation Index (SAVI) and Leaf Area Index (LAI).

3.7.5.1. Normalized Difference Vegetation Index

The Normalized Difference Vegetation Index (NDVI) is ratio of the differences in reflectivity of the near-infrared band (ρ_4) and the red band (ρ_3) to their sum. It is the measure of the amount and vigorsity of vegetation surfaces. The principle behind the NDVI is that green leaves absorb radiation at red wavelengths (640-670nm) due to the presence of chlorophyll pigments. The magnitude of NDVI is related to the level of photosynthesis activity of the observed vegetation. In general, higher NDVI values indicate greater vigour and amounts of vegetation. Values for NDVI range between -1 and +1. Green surfaces have a NDVI between 0 and 1 and water and cloud have negative NDVI values. As the NDVI of the basin (figure 3.7) image shows, the water bodies (i.e. Lake and irrigation dams) have negative NDVI value which ranges between -0.59 to 0 and the vegetation cover has about 0.76 NDVI value.

$$NDVI = \frac{\rho_4 - \rho_3}{\rho_4 + \rho_3} \quad \text{..... (3.9)}$$

Where; ρ_4 and ρ_3 are reflectivities of the near-infrared band and the red band respectively.

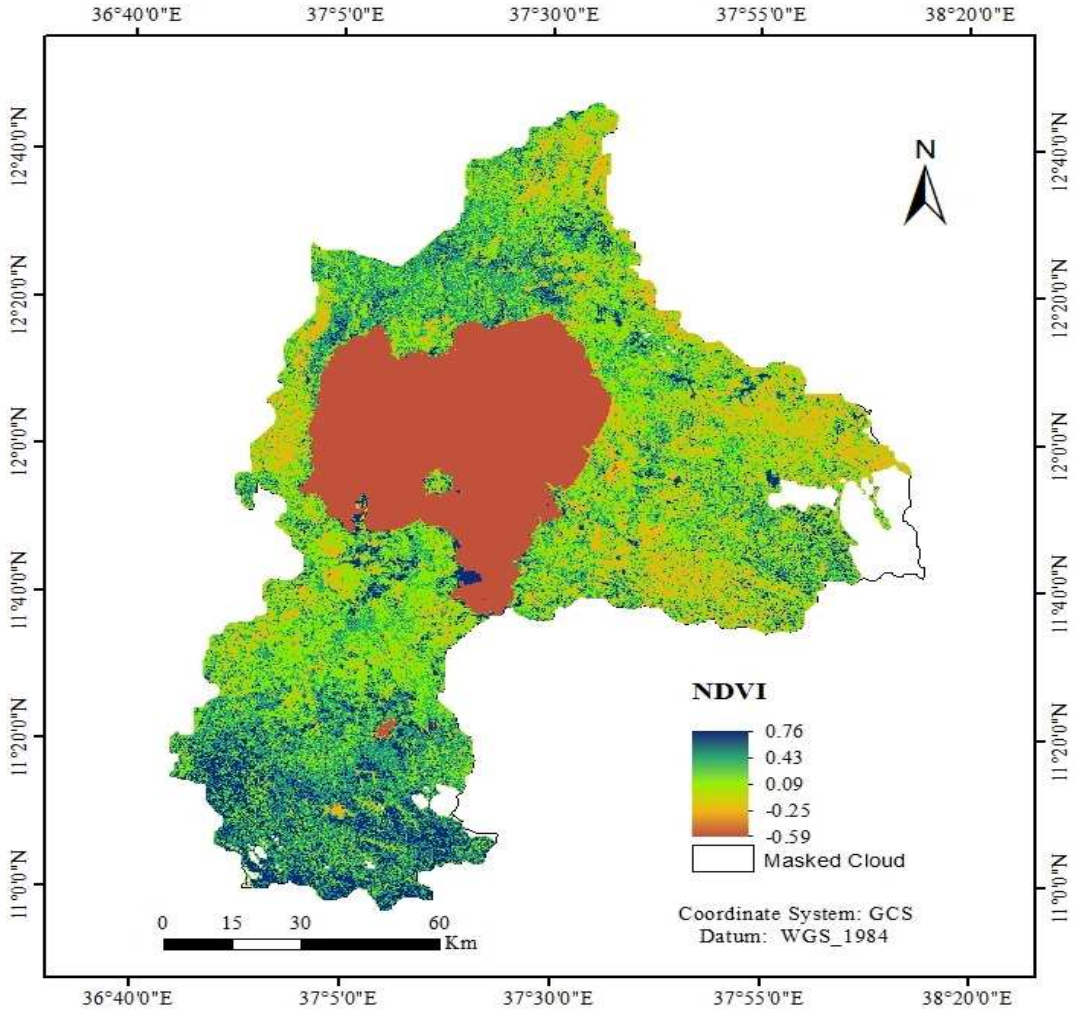

Figure 3.7. Normal difference vegetation index

3.7.5.2. Soil Adjusted Vegetation Index

SAVI is the Soil Adjusted vegetation Index that attempts to "subtract" the effects of background soil from NDVI and the impacts of soil wetness reduced in the index. It can be computed as:

$$SAVI = \frac{(1+L)(\rho_4-\rho_3)}{(L+\rho_4+\rho_3)} \quad \text{..... (3.10)}$$

Where, L is a non-dimensional correction factor which ranges from 0 for high vegetation cover to 1 for very low vegetation cover. The most widely used value is 0.5 which represents an intermediate vegetation densities or known soils types. The SAVI of the basin ranges between -0.24 to 0.57 as shown in figure 3.8.

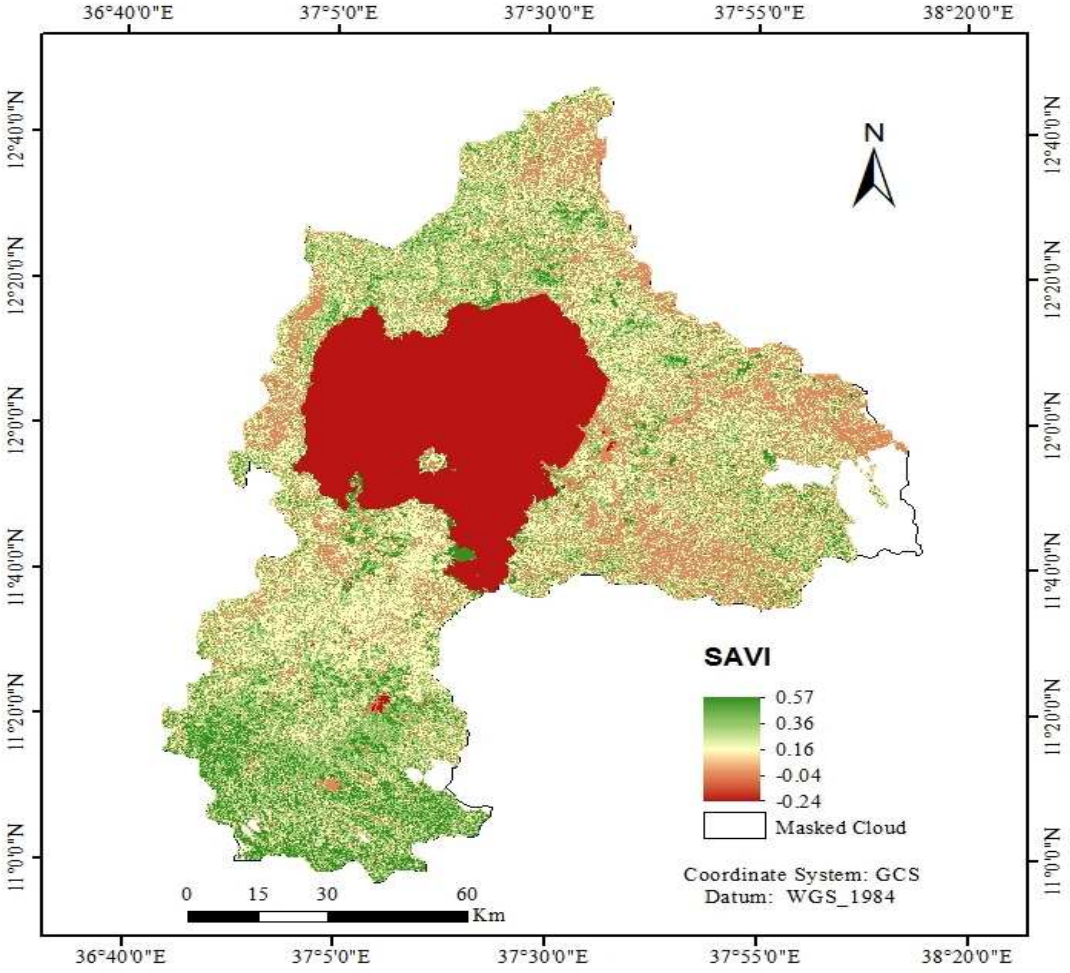

Figure 3.8. Soil adjusted vegetation index

3.7.5.3. Leaf Area Index

Leaf Area Index is the ratio of the total area of all leaves on a plant to the area of the ground covered by the plant. It represents the total biomass of the plant and an indicator of crop yield and canopy resistance to heat flux. LAI can be computed using the following equation.

$$\text{LAI} = -\frac{\ln(0.69 - \text{SAVI}/0.59)}{0.91} \quad \text{..... (3.11)}$$

Where, SAVI is the soil adjusted vegetation index

3.7.5.4. Surface Emissivity

Surface emissivity (ε) is the rate of thermal energy radiation of a surface with related to the black body radiation at the same temperature. It is ratio of the thermal energy radiated by the surface to the thermal energy radiated by a black body at the same surface temperature. There are two types of surface thermal energy emissivities. These are the narrow band 6 (10.4 to

12.5 μm) surface thermal emission (ε_{nb}) and the broad band 6 (6 to 14 μm) surface thermal emission (ε_o) and the first used to calculate the surface temperature (Ts) and the later used to calculate the total longwave radiation ($R_{L\uparrow}$) emission of the surface. Surface emissivities can compute using the vegetation indexes (NDVI and LAI) of the surface based on the following equations.

When NDVI > 0 and LAI < 3, then:

$\varepsilon_{nb} = 0.97 + 0.0033\ LAI$ .....(3.12)

$\varepsilon_o = 0.95 + 0.01\ LAI$ .....(3.13)

For water bodies the NDVI < 0 and $\alpha < 0.47$ and the surface emisssivitie become $\varepsilon_{nb} = 0.99$ and $\varepsilon_o = 0.985$.

3.7.6. Surface Temperature

Instantaneous surface temperature is derived from the spectral radiance of the thermal band using the thermal emissivity behaviour of the surface (ε_o).

$$T_s = \frac{K_2}{\ln\{(\varepsilon_{NB} * K_1 / R_c) + 1\}} \quad \text{..... (3.14)}$$

Where, Ts is the surface temperature in Kelvin, K_1 and K_2 are the thermal band calibration constants of Landsat image shown in table 3.8, ε_{NB} is the narrow band thermal emissivity of the surface and Rc is the corrected thermal radiance from the surface using the spectral radiance of the thermal band. The surface temperature of the basin that extracted from the image ranges between 289 to 315^0K and figure 3.9 shows the surface temperature of the basin.

Table 3.8. Thermal band calibration constants of Landsat 5 TM satellite

Satellite	K1	K2
Landsat 5 TM	607.76	1260.56

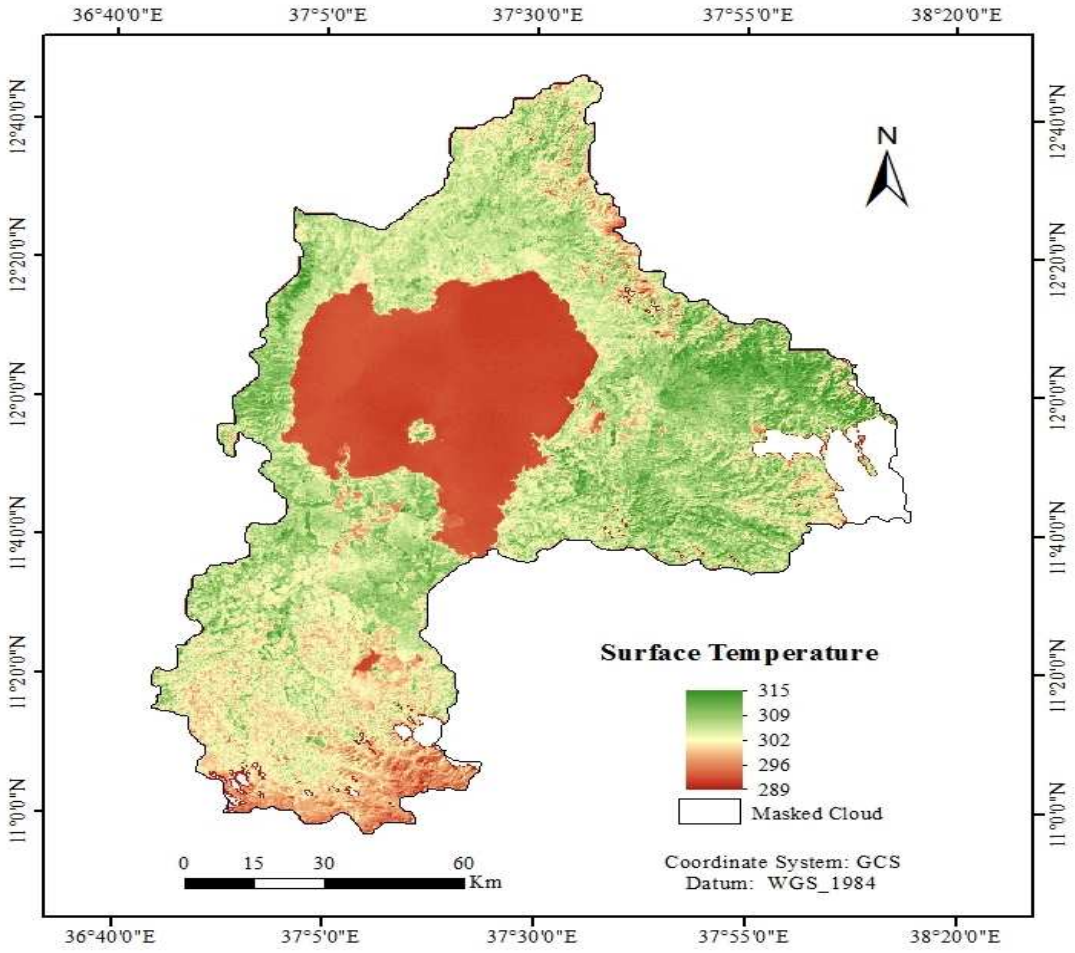

Figure 3.9. Surface temperature

3.7.7. Outgoing Longwave Radiation

The process of emission of long wave radiation from the earth surface to the atmosphere and outer space plays a vital role in surface temperature regulation of the Earth. This long wave radiation emitted from the earth is the total long wave radiation lost from the earth surface. It is the function of the thermal emission potential of the surface and temperature of the surface. It is computed using the Stefan Boltzmann equation.

$R_{L\uparrow} = \varepsilon_o * \sigma * Ts^4$ ..... (3.15)

Where; ε_o is the "broad-band" surface emissivity (dimensionless), σ is the Stefan Boltzmann constant (5.67×10^{-8} $W/m^2/K^4$), and T_s is the surface temperature (K).

3.7.8. Incoming Longwave Radiation

The radiation that emit from the solar system comes to the atmosphere and the earth surface in a wider wavelengths including both the shortwave and long wave radiation. For SEBAL the incoming long wave radiation is the downward thermal radiation flux originated from the atmosphere. The incoming long wave radiation ($R_{L\downarrow}$) is computed using a modified Stefan-Boltzmann equation with atmospheric transmissivity and a selected surface reference temperature.

$$RL\downarrow = \varepsilon_a * \sigma * T_a^4 \quad (3.16)$$

Where; ε_a is the atmospheric emissivity (dimensionless), σ is the Stefan-Boltzmann constant (5.67×10^{-8} $W/m^2/K^4$), and T_a is the near surface air temperature (K). According to Bastiaanssen (1995) the following equation is applied for ε_a.

$$\varepsilon_a = 0.85 * (-\ln \tau_{sw})^{0.09} \quad (3.17)$$

Where, τ_{sw} is the atmospheric transmissivity and by substitution of equation (3.17) to equation (16):

$$RL\downarrow = 0.85 * (-\ln \tau_{sw}) * \sigma * T_{cold} \quad (3.18)$$

Where, τ_{sw} is the atmospheric transmissivity and T_{cold} is the substitution of the cold pixel temperature for Ta and it is considered as the estimation of the coming long radiation for a green standard surface alfalfa.

3.8. Surface Energy Balance Calculations

The Earth is relatively close to an energy balance system which implies an equal amount of energy enters into the Earth system and releases out of it (Liou and Kar, 2014). Surface energy balance is the balance among energy absorbed, reflected and emitted by the earth surface.

3.8.1. Net Radiation Flux

According to the physical laws of radiation balance, the net radiation can be considered as a balance between incoming and outgoing short wave and long wave radiation on the Earth surface. The net radiation flux at the surface (Rn) represents the actual radiant energy available at the surface for warming the soil, air and evaporating water from soil, vegetation

and water bodies. It can be computed by subtracting all outgoing radiant fluxes from all incoming radiant fluxes.

$R_n = (1 - \alpha) RS_{\downarrow} + R_{L\downarrow} - R_{L\uparrow} - (1-\varepsilon_o) R_{L\downarrow}$ ..... (3.19)

Where, $R_{S\downarrow}$ is the incoming shortwave radiation (W/m^2), α is the surface albedo (dimensionless), $R_{L\downarrow}$ is the incoming long wave radiation (W/m^2), $R_{L\uparrow}$ is the outgoing long wave radiation (W/m^2), and ε_o is the surface thermal emissivity (dimensionless). The term $(1-\varepsilon_o) RL_{\downarrow}$ represents the fraction of incoming long wave radiation that is lost from the surface due to reflection.

The amount of short wave radiation that remains available at the surface is a function of the surface albedo. Surface albedo is the reflection coefficient defined as the ratio of the reflected radiant flux to the incident radiant flux over the solar spectrum. It is calculated using satellite image information on spectral radiance for each satellite band. The incoming shortwave radiation is computed using the solar constant, the solar incidence angle, relative earth distance and computed atmospheric transmissivity. The incoming long wave radiation is computed using the modified Stefan-Boltzmann equation with atmospheric transmissivity and a selected surface reference temperature. Outgoing long wave radiation is computed using the Stefan-Boltzmann equation with a calculated surface emissivity and surface temperature. The surface temperature is computed from the satellite image information on thermal radiance. The surface emissivity is the ratio of the actual radiation emitted by the surface to that emitted by a black body at the same surface temperature. In SEBAL Model, surface emissivity is computed as a function of vegetation index (Giridhar and Suneel, 2014). For the computation of the above surface radiation balance equation (3.19) SEBAL Model uses series of steps (Figure 3.10) using the ERDAS Model Maker.

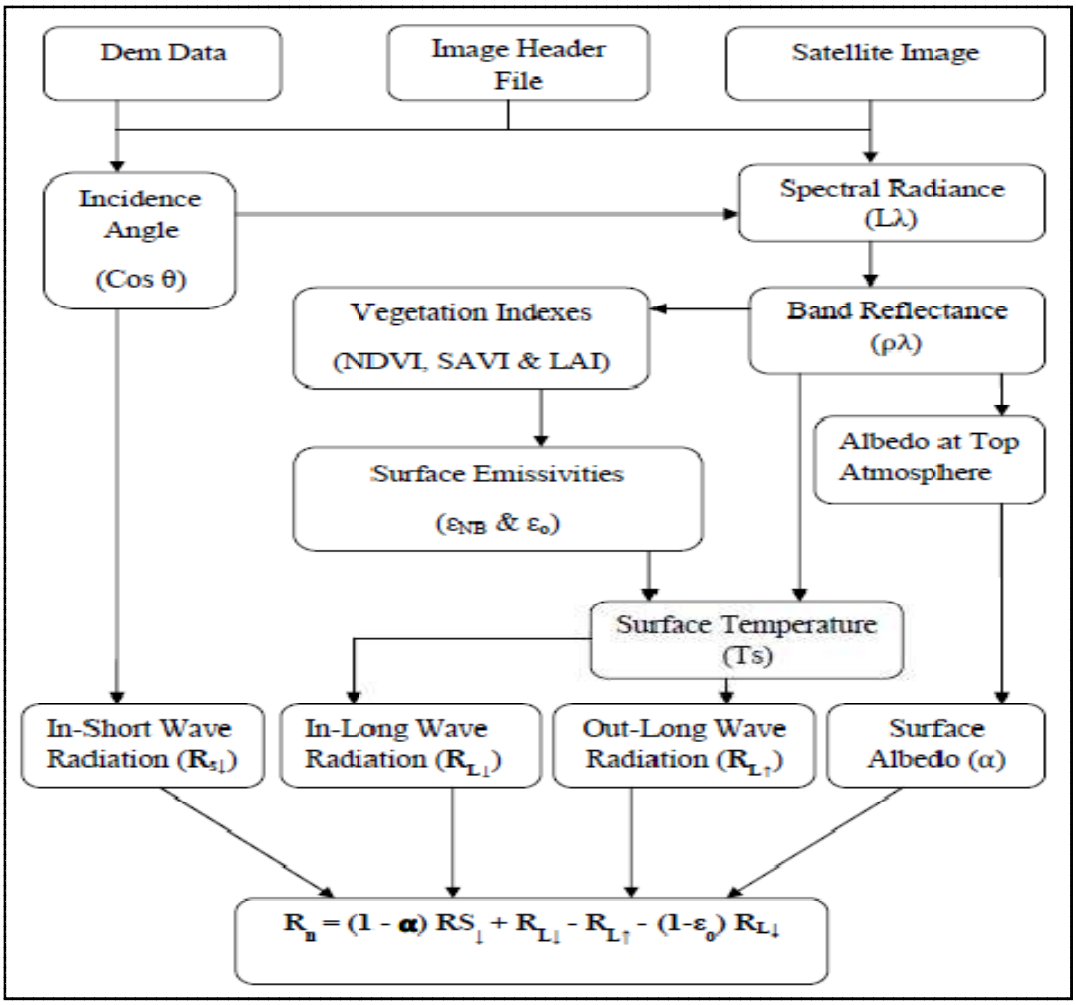

Figure 3.10. Method of solving net radiation flux modified from Mendonca et al. (2012)

3.8.2. Soil Heat Flux

Soil heat flux (G) is the part of net radiation energy lost to heat the ground surface (soil and vegetation) by conduction. It is high dependent on the available soil moisture and vegetation cover of the surface. Soil heat flux is usually measured with sensors that can measure rate of heat conductivity nature of the soil. In remote sensing, it is not possible to measure the direct soil heat flux and it is indirectly calculated using vegetation indices, surface temperature, and surface albedo (Bastiaanssen, 2000).

$$G = R_n \left(\frac{T_s}{\alpha}\right) * (0.0038\alpha + 0.0074\alpha^2) * \left(1 - 0.98NDVI^4\right) \quad \text{..... (3.20)}$$

Where, G is soil heat flux, Rn is the net radiation, Ts is the surface temperature in Kelvin, α is the surface albedo and NDVI is the normalized difference vegetation index. The soil heat flux that used to warm the soil of the basin ranges between 0 to 80W/m2 as shown in figure 3.11.

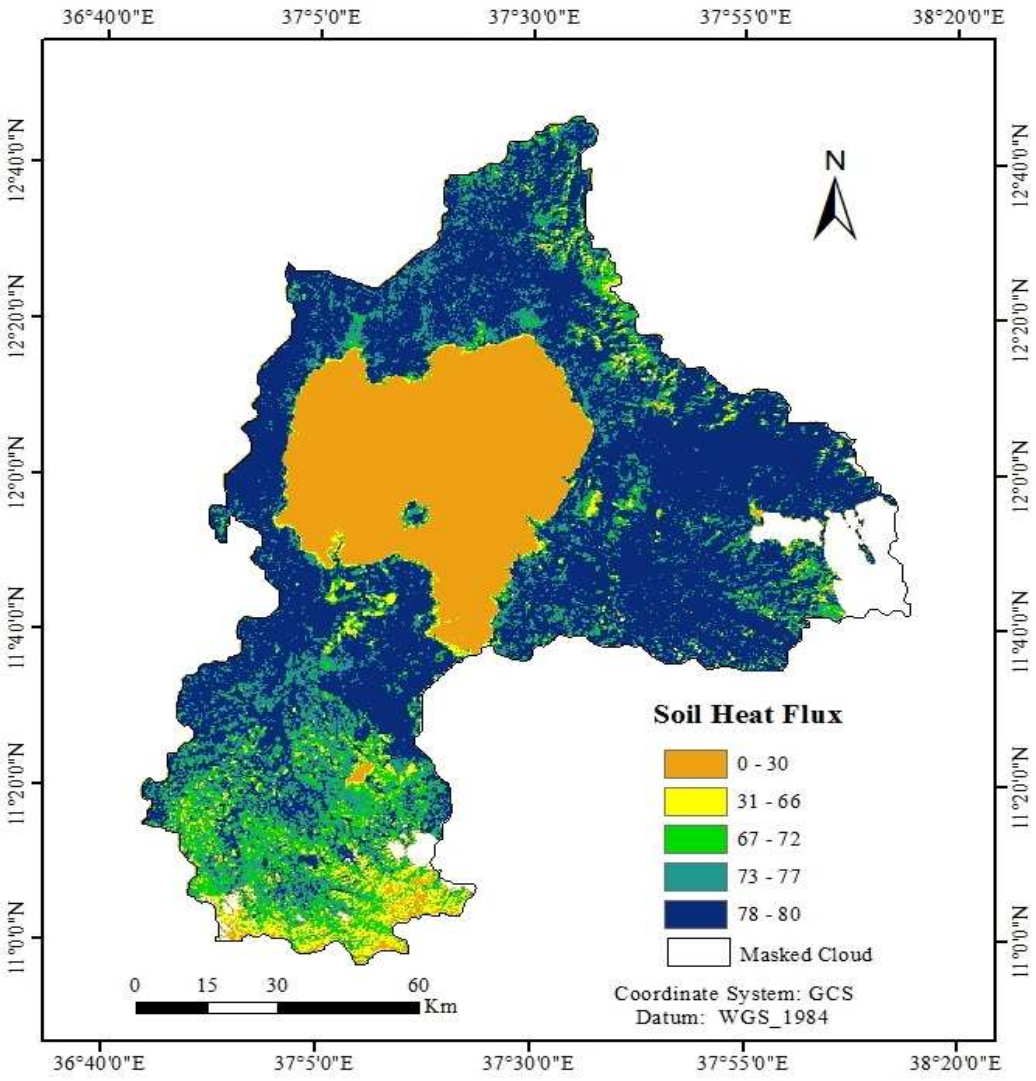

Figure 3.11. Soil heat flux

3.8.3. Sensible Heat Flux

Sensible heat flux (H) is the rate of heat energy loss from surface to the atmosphere via conduction process due to the temperature difference between the surface and lower atmosphere. The rate of sensible heat transfer is dependent on the wind speed, surface roughness length and surface to air temperature differences. It is computed using the heat and momentum transport equation.

$$H = \rho_{air} C_{\rho} * \left(\frac{T_s - T_a}{r_{ah}}\right) \quad \text{..... (3.21)}$$

Where; ρ_{air} is air density (kg/m^3), c_p is air specific heat (1004 J/kg/K), Ts is the surface temperature, T_a is the air temperature and r_{ah} is the aerodynamic resistance to heat transport

(s/m). The above equation is difficult to solve due to the unknown values of the temperature difference (Ts - Ta) between the two heights (z_1 and z_2) and the aerodynamic resistance (rah) for heat and vapour transport to the atmosphere.

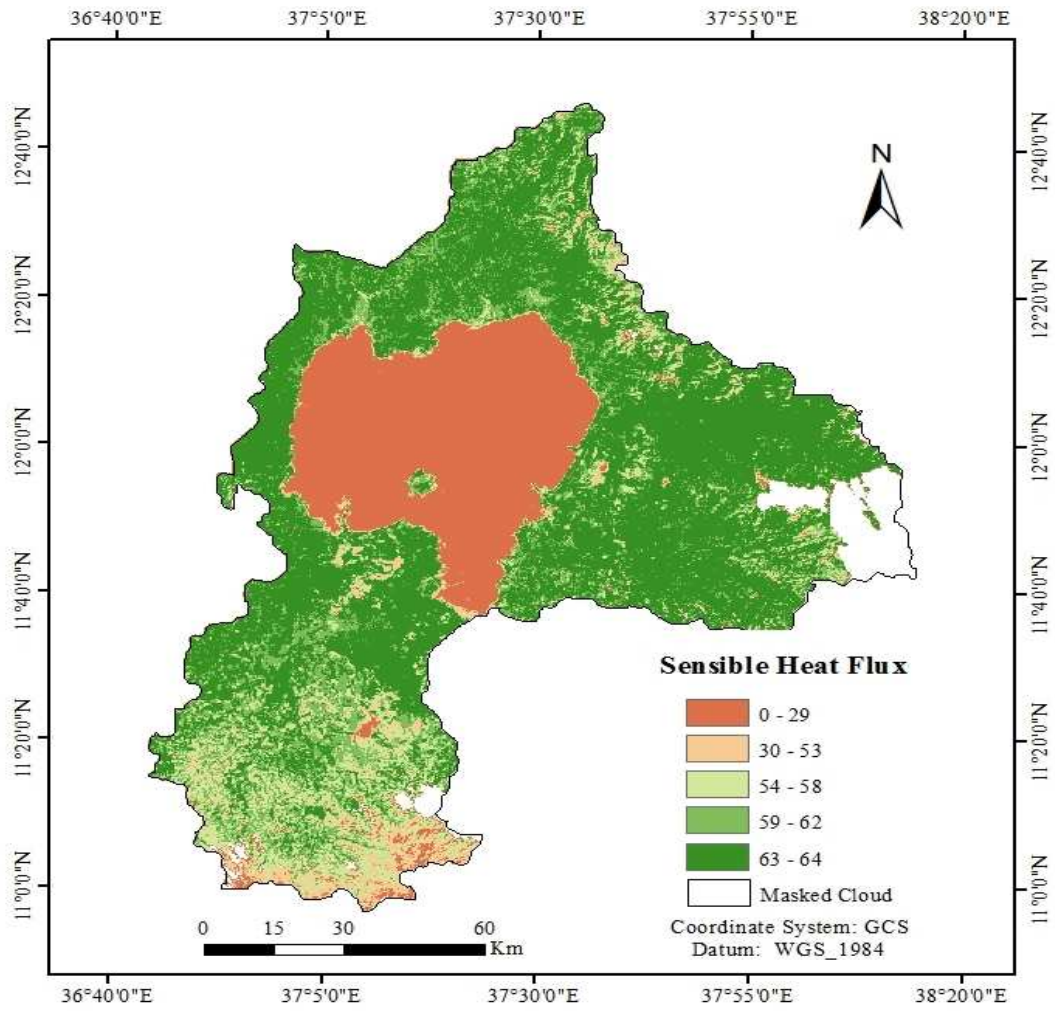

Figure 3.12. Sensible heat flux

3.8.3.1. Temperature Difference

In SEBAL model, the evapotranspiration of the enter image is computed based up on the two extreme conditions found within the image. First, extreme high evapotranspiration pixel assumed that all available energy is consumed as a latent heat without limitation of moisture and the loss of energy as a sensible heat is considered as negligible (i.e. cold pixel). The cold pixel has the lowest surface temperature value within the image and found on the deep water bodies or relatively on a well saturated alfalfa grass land. Second, extreme low evapotranspiration pixel assumed that all the available energy is lost as a sensible heat and

loss of energy as latent heat is considered as zero due to the absence of moisture (dry pixel). The dry pixel has the highest surface temperature within the image and found on fully dry bare land. The selection of these two anchor pixels (i.e. cold/wet and hot/dry) requires a serious attention and practice. The full guideline on the selection of the anchor pixels is available on Allen et al. (2001).

For the computation of the sensible heat flux, the near surface temperature difference for each pixel needs to be defined. However, the air temperature at each pixel is unknown and SEBAL uses the two anchor pixels (i.e. cold pixel and the hot pixel) where the reliable values of H can be predicted and dt can estimate. After the selection of these anchor pixels, the surface energy flux parameters such as net radiation, soil heat flux, aerodynamic resistance and surface temperature values are recorded that used to compute the temperature difference at these pixels (see equation 3.23 and 3.24). Finally, by using the temperature difference at these anchor pixels and their corresponding surface temperature, the correlation coefficients that determine the linear relationship between the surface and air temperatures "a" and "b" are computed as described below.

SEBAL computes dT for each pixel by assuming a linear relationship between dT and the surface temperature (T_s).

$dT = aTs + b$ .....(3.22)

Where Ts is the surface temperature and "a" and "b" are the correlation coeffients obtained from the "anchor" pixels (Bastiaanssen, 1995).

The anchor pixels represent conditions of extreme evaporative behaviour within the image. The cold pixel represents the lower surface temperature on the image that indicates wet condition. In cold pixel, most of the available energy (Rn-G) is consumed by evapotranspiration and the sensible heat flux (H) and near surface air temperature difference (dT) assumed to be near zero. However, the sensible heat flux at the cold pixel can be calculated as;

$H_{cold} = Rn_{cold} - G_{cold} - \lambda ET_{cold}$ and the near surface temperature difference at the cold pixel can be computed as;

$$dT_{cold} = \frac{H_{cold} * r_{ah\_cold}}{\rho_{cold} * C_{\rho}} = \frac{(Rn_{cold} - G_{cold} - \lambda ET_{cold}) * R_{ah\_cold}}{\rho_{cold} * C_{\rho}} \quad \text{..... (3.23)}$$

Where, H_{cold}, Rn_{cold}, G_{cold}, and ET_{cold} are values of sensible heat, net radiation, soil heat flux, and evapotranspiration, respectively, for the cold pixel.

Based on research experience, most cold pixel (wet agricultural fields) have an ET rate about 5% larger than the reference ET (ET_o) and ET_{cold} assumed to be 1.05*ETo (Allen et,al. 2011). Similarly, the "dry pixel" represents the pixel with high surface temperature and lack of available moisture for evapotranspiration. Therefore, ET_{hot} is assumed to be zero for a dry agricultural field having no green vegetation and with dry soil surface layer. As result, all the available energy is considered as directly converted to sensible heat and lost as conduction to the atmosphere. Hence, the sensible heat flux can be calculated as; $H_{hot}= Rn_{hot} - G_{hot}$ and the near surface temperature difference also can be computed as;

$$dT_{hot} = \frac{H_{hot} * R_{ah\_hot}}{\rho_{hot} * C_{\rho}} = \frac{(Rn_{hot} - G_{hot}) * R_{ah\_hot}}{\rho_{hot} * C_{\rho}} \quad \text{..... (3.24)}$$

Where, H_{hot},Rn_{hot},ET_{hot} and G_{hot} are sensible heat flux, net radiation, evapotranspiration and soil heat flux respectively for the hot pixel. Finally, the correlation coefficients a and b can be calculated as;

$$a = \frac{dT_{hot} - dT_{cold}}{T_{s\_hot} - T_{s\_cold}} \text{ and } b = dT_{hot} - aT_{s\_hot} \quad \text{..... (3.25)}$$

where, dT_{hot} and dT_{cold} are dT values of hot and cold pixels respectively and Ts_{hot} and Ts_{cold} are the corresponding surface temperature values of of the hot and cold pixels respectively.

3.8.3.2. Momentum Roughness Length

Surface roughness refers to the unevenness and undulated nature of the earth surface due to the natural processes like topography and vegetation or human activities such as the construction of buildings, power lines. It can be defined as the aerodynamic roughness length (height) above the surface at which the wind profile is assumed to be zero. Surface roughness affects the transfer of heat and vapour from the earth surface to the atmosphere and it is considered as the measure of drag and skin friction of the surface for the layer of air that interacts with surface. It is important input to estimate the wind speed, friction velocity and aerodynamic resistance (rah). It can be estimated from the average vegetation height (m) of the area of interest using the following equation.

$Z_{om} = 0.12\ h$..... (3.26)

The above equation requires the known heights of vegetation cover of the area of interest and not appropriate for wider areas i.e. regional scale that characterized by various land cover types which are difficult to estimate the average heights of all vegetations. According to Bastiaanssen (2000), the surface roughness length is estimated more accurately using the NDVI and surface albedo of the area that derived from remotely sensing data. The use of surface albedo (α) helps to distinguish between some tall and short vegetation types that may have similar NDVI values. For this research, the roughness length of the basin is computed from the NDVI and surface albedo using the following empirical equation:

$$z_{om} = \exp\left\{\left(a * \frac{NDVI}{\alpha}\right) + b\right\} \quad \text{..... (3.27)}$$

Where, a and b are correlation constants derived from a plot of $\ln(Z_{om})$ versus NDVI/α for two or more sample pixels representing specific vegetation types.

3.8.3.3. Friction Velocity

Friction velocity (m/s) is the area-average wind speed at the blending height that quantifies the turbulent velocity fluctuation in the air. The blending height is the height above the weather station at 200m elevation that one can assume no effect of surface roughness on heat and momentum transfer. The wind speed increases while the friction velocity deceases with height due to the reduction of the effect of surface roughness. The wind speed at the blending height that assumed to be constant for all pixels of the image is used since it is not affected by the surface features. Friction velocity at the blending height is important to calculate the aerodynamic resistance to heat transfer between the surface and atmosphere.

The friction velocity at 2 meter height that derived from the wind data of weather stations used to calculate the wind speed at the blending height and it can computed using the following equation:

$$u^* = \frac{ku_x}{\ln(2/z_{om})} \quad \text{..... (3.28)}$$

Where; k is von Karman's constant, u_x is the wind speed (m/s) at 2 meter height, and z_{om} is the momentum roughness length. Using the friction velocity computed from the above equation, wind speed at the blending height can be computed using the following equation:

$$u_{200} = u^* \frac{\ln(200/z_{om})}{k} \quad \text{..... (3.29)}$$

Where, U_{200} is wind speed at blending height of 200m, U* is the friction velocity at the weather station. Friction velocity is computed using the logarithmic wind law for neutral atmospheric conditions through rearranging the above equation.

$$u^* = \frac{ku_{200}}{\ln(200/z_{om})} \quad \text{..... (3.30)}$$

Where; k is von Karman's constant, u_{200} is the wind speed (m/s) at the blending height of 200m, and z_{om} is the momentum roughness length.

3.8.3.4. Aerodynamic Resistance

Aerodynamic resistance refers to the effects of features above the surface and the over flowing air (i.e. advection and air turbulent) on the transfer of heat and vapour to the atmosphere. According to FAO (2006) the term resistance includes two factors of surface resistance and aerodynamic resistance. The former resembles the bulk resistance which describes the resistance of vapour and heat flow through stomata openings, total leaf area and soil surface and the later describes the resistance from the vegetation upward and involves friction from air flowing over vegetative surfaces. The temperature gradient between two known heights above the surface (Z_1 and Z_2) and the aerodynamic resistance to heat transport between this heights used to compute the sensible heat flux in surface energy balance algorithms. It can be computed using the following equation.

$$R_{ah} = \frac{\ln(z_2/z_1)}{u^*k} \quad \text{..... (3.31)}$$

Where, z_1 and z_2 are the heights above the surface where the temperature gradient is defined, U* is friction velocity (m/s) and k is the Karman's constant (0.41).

A series of iterations is required to determine the value for rah for each period that considers the impacts of instability (i.e., buoyancy) on rah and H. Assuming neutral atmospheric conditions, an initial r_{ah} is computed using Equation (3.30). Z_1 is the height just above the zero plane displacement (d ≅ 0.67 × height of vegetation) for the surface or crop canopy and z_2 is some distance above the zero plane displacement, but below the height of the surface boundary layer. Based on experienced analysis, values of 0.1 meter for z_1 and 2.0 meters for z_2 are assigned.

3.8.4. Latent Heat Flux

Latent heat flux (vapor transference to the atmosphere) was computed by the simple difference between the net radiation, soil heat flux and sensible heat flux. It was computed by rearranging equation 3.1 as follows:

$\lambda ET = Rn - G - H$ ..... (3.32)

where: λET represents the latent heat flux, Rn is the net radiation and G is the soil heat flux, all expressed in W/m^2.

3.9. Hourly Actual Evapotranspiration

Hourly actual evapotranspiration is the combined rate of water loss occur both from the soil and vegetation surface under the existing available soil moisture and weather condition. It has been computed as a residual in water balance equations by computing the potential evapotranspiration (ETo) or indirectly from field measurements. Actual field measurements and calculations based up on standard meteorological data were explained by FAO (2006).

Hourly actual evapotranspiration can be obtained using satellite remote sensing techniques. These methods provide a powerful means to estimate the different surface energy fluxes and to compute actual evapotranspiration from pixel to an entire basin scale. The Surface Energy Balance Algorithm for Land (SEBAL Model) is one of the widely used surface energy balance model that provides accurate estimation of actual evapotranspiration using satellite imagery and meteorological data for the satellite over pass time.

After the computation of the latent heat flux for the satellite over pass time, the equivalent instantaneous (hourly) evapotranspiration is computed using the following equation:

$$ET_{inst} = 3600 * \frac{\lambda ET}{\lambda} \quad \text{..... (3.33)}$$

Where, ET_{inst} is the instantaneous ET (mm/hr), 3600 is the time conversion from seconds to hours and λ is the latent heat of vaporization which equivalent to $2.45*10^6$ J/kg.

3.10. Reference Evapotranspiration

The reference evapotranspiration (ETo) is the rate of evapotranspiration from a hypothetical growing green grass which actively growing and completely cover the ground in a well water saturated field under a given climatic condition. It is the average or standard

evapotranspiration rate of water from a representative surface. It provides the evaporative demand of the atmosphere independently of the crop type, growth and development stage and management practices. The only factors affecting ETo are climatic parameters. Consequently, ETo is a climatic parameter and can be computed from weather data. ETo expresses the evaporating power of the atmosphere at a specific location and time of the year and does not consider the crop characteristics and soil factors.

The FAO Penman-Monteith method is recommended as the sole method for determining ETo. The method has been selected because it closely approximates grass ETo at the location evaluated, is physically based, and explicitly incorporates both physiological and aerodynamic parameters. Moreover, procedures have been developed for estimating missing climatic parameters and it is considered as a standard method of computing the refernce evapotranspiration. In this study, FAO Penman Montieth method is used to compute the refence evapotranspiration (ETo) using the following equation.

$$ET_o = \frac{0.408\Delta(R_n - G) + \gamma\frac{900}{T+273}U_2(e_s - e_a)}{\Delta + \gamma(1 + 0.34U_2)} \quad \text{.....(3.34)}$$

Where, ETo is refernce evapotranspiration, Rn is net radiation at the surface, G is the soil heat flux, T is the mean daily air temperature, U_2 is the wind speed at 2 meter height, es is the saturation vapor pressure, ea is the actual vapour pressre, es - ea is the saturation vapour pressere deficit, Δ is the slope of the vapour pressure curve and γ is the psychrometic constant.

The computation of all parameters put in above equation followed the method and procedure given in FAO Irrigation and Drainage Paper 56 and computed with spreadsheet. Daily ETo were computed by the FAO Penman–Monteith formula based on the weather data i.e. temperature, sunshine hours, wind speed and relative humidity of the weather stations.

3.11. Evapotranspiration Fraction

Evaporative Fraction is the ratio of the computed instantaneous ET (ET_{inst}) for each pixel to the reference ET (ETo) computed from weather data. It is similar to a well known crop coefficient and used to extrapolate ET from the imaging time to 24 hour or longer periods. Generally, ETrF values range from 0 to 1 and assumed to be constant during the day depending up on the self preservation process in main surface energy balance components on

the daily basis. At a totally dry pixel, ET = 0 and ETrF = 0. A pixel in a well established field of alfalfa or corn can occasionally have an ET slightly greater than ET_o and therefore ETrF > 1, perhaps up to 1.1. However, ET_o generally represents an upper bound on ET for large expanses of well-watered vegetation. The evaporative fraction can be computed using the following equation.

$$ETrF = \frac{ET_{inst}}{ET_o} \quad \text{..... (3.35)}$$

Where ETrF is the evaporative fraction, ET_{inst} is the actual and ETo is the reference evapotranspirations respectively for the satellite imaging time.

The evaporative fraction also can be computed using the relationship between the latent heat flux, net radiation and soil heat flux in the absence of instantaneous reference evapotranspiration data of the required area using the following empirical equation (Allen et al., 2011).

$$EF = \frac{\lambda ET}{(R_n - G)} \quad \text{..... (3.36)}$$

Where EF is the evaporative fraction, λET is the latent heat flux, Rn is the net radiation and G is the soil heat flux corresponding to the satellite over pass time.

3.12. Daily Evapotranspiration

The daily evapotranspiration is the depth of water (mm/day) lost as a vapour to the atmosphere during the 24 hours of a day from the soil, water and vegetation surfaces. SEBAL computes the instantaneous energy fluxes and evapotranspiration for the satellite overpass time. These instantaneous values then extrapolated to daily and long period values by using the evaporative fraction. Assuming the instantaneous evaporative fraction is equivalent to its daily average value, ET_{24} can be calculated by using the evaporative fraction and reference evapotranspiration (ETo) using the following equation (Allen et al., 2011).

$$ET_{24} = ETrF * ETo_{\_24} \quad \text{..... (3.37)}$$

Where, ET_{24} is the daily evapotranspiration, ETrF is the daily average evaporative fraction and $ETo_{\_24}$ is the daily reference evapotranspiration.

3.13. Seasonal Evapotranspiration

The determination of monthly and seasonal water demand is important in full or supplementary irrigation agriculture and for other water resource management systems. In conventional application methods, it can computed by multiplying the reference evapotranspiration (ETo) that represent the evaporative demand of the atmosphere of the place with the individual crop characteristics (kc). Similarly, in remote sensing methods, the seasonal evapotranspiration of the required area that cover the enter growing season can be computed with the multiplication of the evaporative fraction (ETrF) derived from the satellite images and assumed to be equivalent to crop coefficient (Kc) with the reference evapotranspiration (ETo) computed from weather data. The evaporative fraction computed for the time of the image is also assumed to be constant for the entire growing season and shows the spatial variation in actual evapotranspiration of the study area in relation to the actual variation in land use and land cover characteristics.

The seasonal evapotranspiration is computed by multiplying the ETrF of the time of image with the sum of daily ETo values of the required season period.

$$ET_{season} = \left(ETrF * \sum_{i=1}^{n} ETo_{24}\right) \quad \text{..... (3.38)}$$

Where, ET_{season} is the seasonal evapotranspiration in mm depth of water, ETrF is the evaporative fraction of the image, ETo_{24} is the daily ETo in mm/day and n represent the number of days in the season.

CHAPTER 4 : RESULTS AND DISCUSSION

4.1. Spatial Distribution of Vegetation Cover in the Basin

The land use and land cover of Tana basin was classified using three Landsat satellite images. The basin images were classified using supervised image classification method by taking sample training points from each land use classes and the maximum likelihood parametric rule is used to calculate the probability of each pixel to assign in the right class value.

The land use cover map of the basin also compared with the previous studies conducted in the study area and relatively similar result was obtained. Table 4.1 shows that most of the basin is covered with crop land 41.9%, water body 19.9%, shrub and woody savanna grasslands 30.6% and few scattered forest areas which account only about 0.8% of the total basin area.

Table 4.1. Land use and land cover classes and their areal coverage

No.	Land Use Classes	Area (ha)	Percent (%)
1	Crop land	634939.6	41.9
2	Savanna	462854.1	30.6
3	Water Body	301851	20.0
4	Forest areas	11648.3	0.8
5	Grass Lands	15676.7	1
6	Urban areas	2912.1	0.2
7	Bare Land	26160.8	1.7
8	Masked cloud	58601.9	3.8
9	Total Basin Area	15,14644	100

The vegetation cover is unevenly distributed to the basin and the southern part is covered with vegetation relative to the northern and eastern parts of the basin. The northern and eastern parts of the basin are characterized by agricultural farming areas with a few scattered bushes and woody savanna grass lands. The results of the classified land use and land cover map of the basin are shown in Figure 4.1.

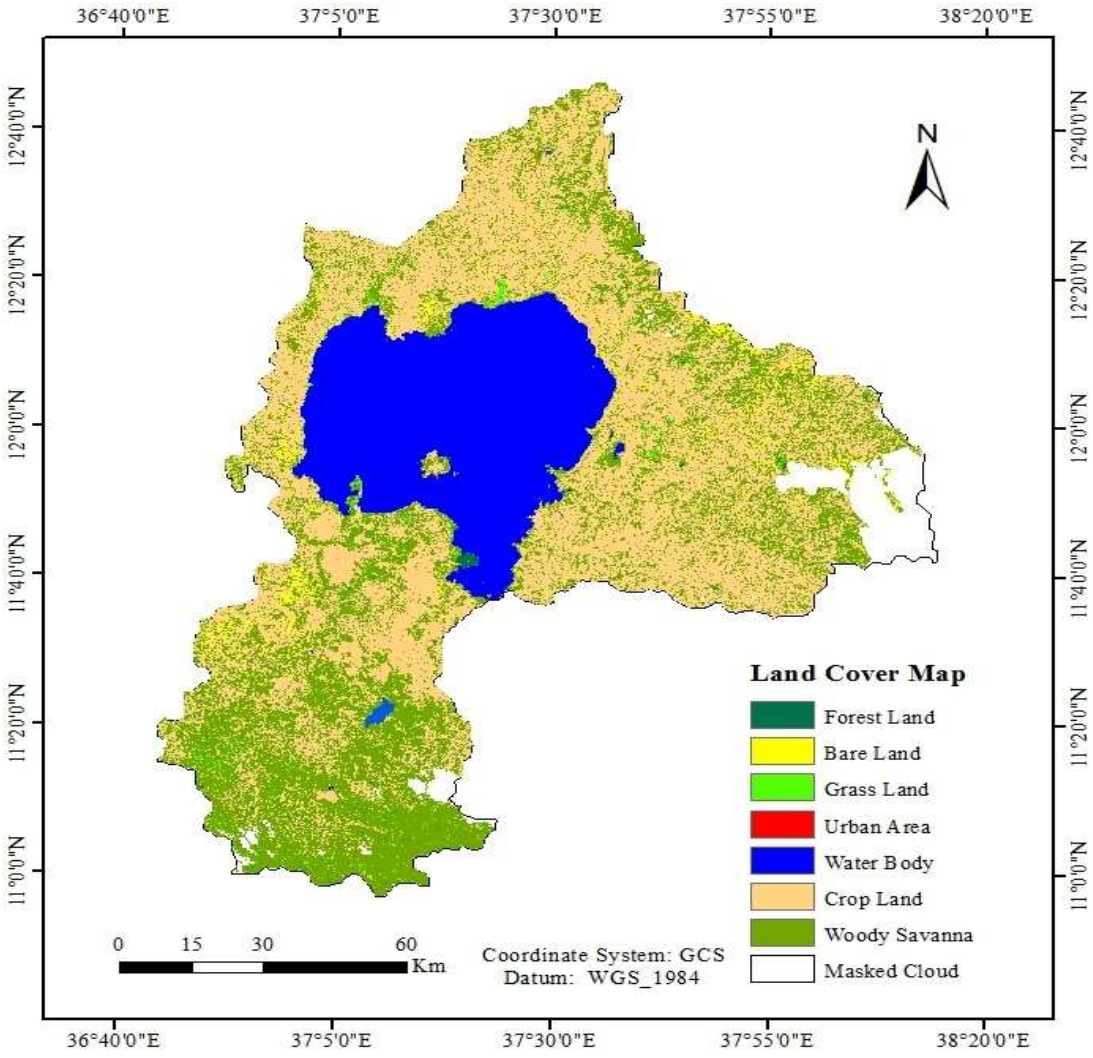

Figure 4.1. Land use and land cover map of Tana Basin

4.2. Spatial Distribution of Evapotranspiration in the Basin

The daily actual evapotranspirtaion of the basin was derived from the satellite images as the residual energy flux of the surface energy budget equation using the surface energy balance algorithm for land (SEBAL Model). The Penman-Monteith method of estimating reference evapotranspiration had also been carried out in daily and monthly bases for deriving actual daily and seasonal evapotranspiration.

4.2.1. Daily Evapotranspiration

The daily actual evapotranspiration (ET_{24}) is more useful than the instantaneous evapotranspiration to adjust the rate of water consumption and for hydrological, ecological and environmental studies. The reference evapotranspiration computed from meteorological

data and evaporative fraction derived from satellite images used to calculate the daily actual evapotranspirtaion of the basin. The evaporative fraction is assumed as equivalent to its average daily value depending on the self preservation of the main daily energy balance components (Allen et al., 2011).

As the different studies (Allen et al., 2007; Ayenew, 2003) have proven that SEBAL can give good estimation of daily evapotranspiration over different land use and land cover classes. The actual evapotranspiration of the basin ranges from 0 to 4.3 mm/day that observed on bare lands and water bodies of the basin, respectively. The large portion of the basin has the range of evapotranspiration between 1.3 to 2.3 mm/day which covered by agricultural crops and grasslands. The actual evapotranspiration is measured between 2.4 to 2.8mm/day in woody savanna grass lands. The maximum amount of daily evapotranspiration is measured on forest lands and water bodies of the basin which is about 2.9 to 4.3 mm/day.

The spatial distribution of basin evapotranspiration is related to the vegetation distribution as shown in figure 4.2. The eastern and western parts of the basin show lower evapotranspiration corresponding to their little or no vegetation cover. However, the southern part of the basin has Eucalyptus plantations and woody savanna bush lands. Hence, the southern (downstream) of the lake shows higher evapotranspiration due to the existing dense vegetation cover.

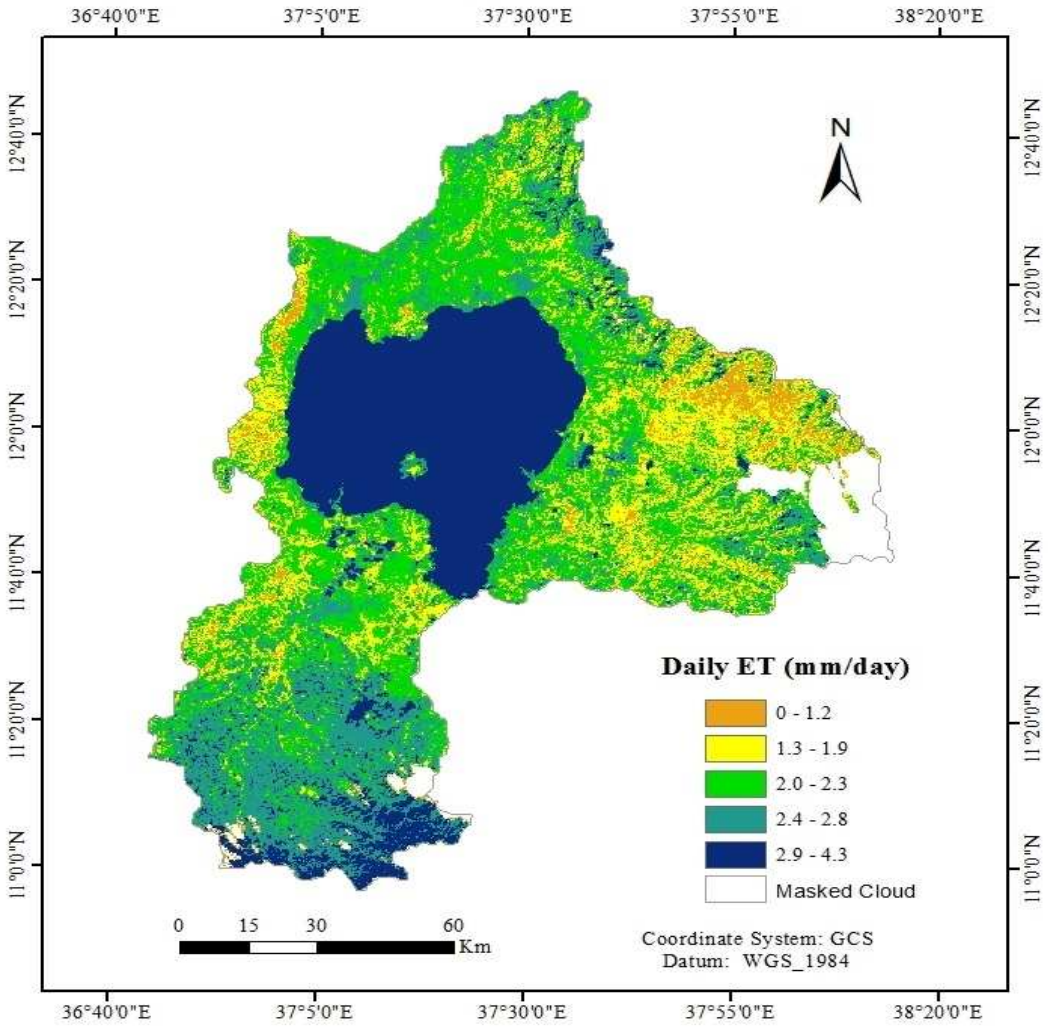

Figure 4.2. Daily evapotranspiration

4.2.2. Seasonal Evapotranspiration

Seasonal evapotranspiration is equivalent to the total amount of consumptive water required to satisfy the water demand of a crop for its full growing season and often used to quantify the total water consumption for agriculture (Allen et al., 2007). The seasonal evapotranspiration map of the basin is generated by the multiplication of the evaporative fraction (EF) derived from the satellite images with the daily reference evapotranspiration (ETo) computed from meteorological data for the required season. The evaporative fraction computed for the time of the image is also assumed to be constant for the entire growing season.

The total dry season (i.e. October to January) evapotranspiration of the basin ranges between 20 to 439 mm that observed on bare lands and water bodies of the basin respectively. Figure

4.3 shows that the dominant part of the basin has total seasonal ET value range from 263 mm to 351 mm depth of water that is covered with agricultural crops and grasslands. The water bodies and forest areas have the maximum ET value of about 439 mm depth of water.

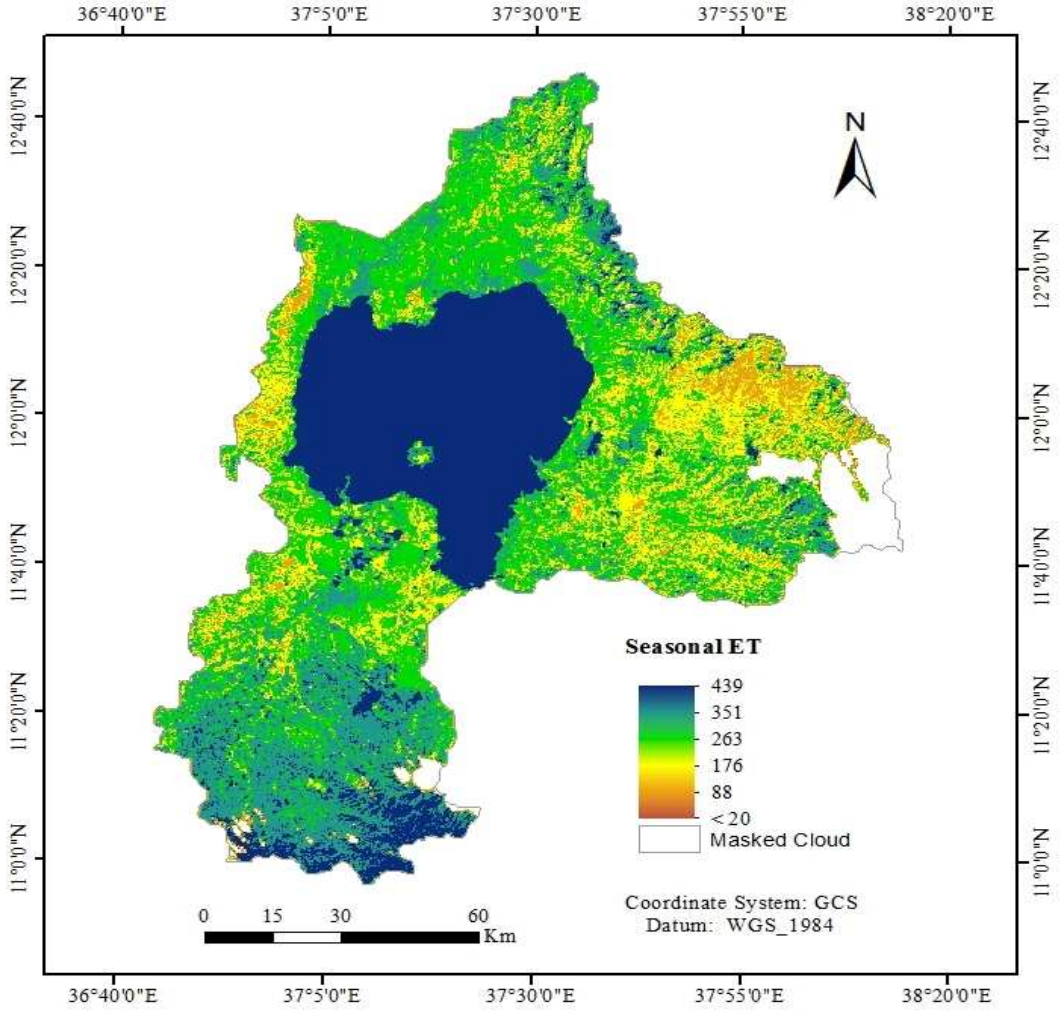

Figure 4.3. Seasonal evapotranspiration

4.3. Comparison of Surface Flux Parameters

The main purpose of comparison is to deterimine the relationship exist between the surface flux parameters and to show the influence of one parameter on the other. Hence, the comparison of surface flux model results against each other and against ground based measurements provide information for model validation and helps to draw conclusion depend up the model results.

4.3.1. Surface Temperature and Daily Evapotranspiration

Evapotranspiration is the function of surface and air temperatures, solar radiation, humidity and wind condition which affect the process of evapotranspiration. Moreover, temperature affects evapotranspiration by increasing the vapour holding capacity of the air. Hence, low evapotranspiration occurs in a condition of low temperature (Kosa, 2011).

The results of the model (i.e. surface temperature and daily evapotranspiration) were compared to show the effect of surface temperature on the occurence of daily ET as shown in figure 4.4. The result of the line graph shows that there is a linear relationship between surface temperature and daily evapotranspiration.

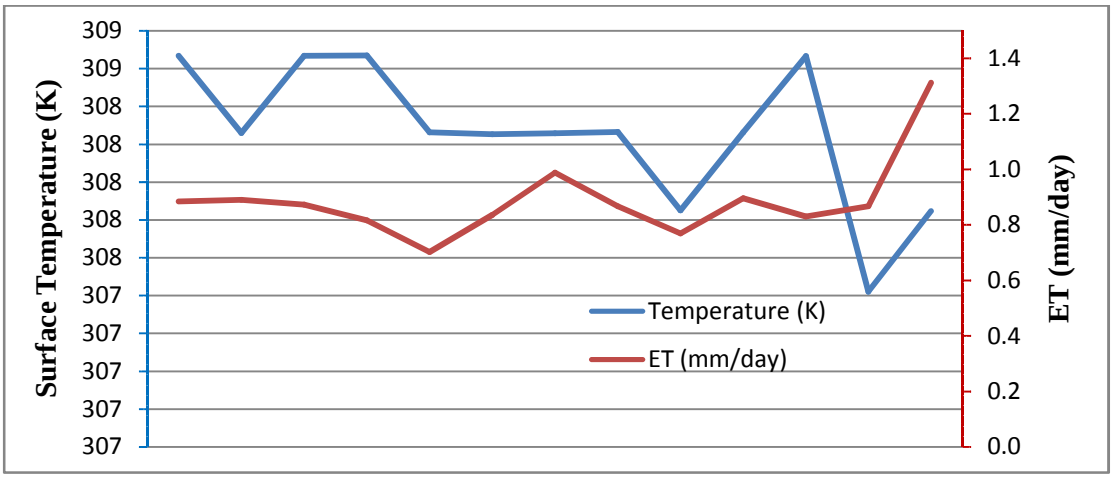

Figure 4.4. Line graph of surface temperature and daily evapotranspiration

4.3.2. NDVI and Daily Evapotranspiration

The spatial distribution of vegetation cover within the basin has a direct control on the distribution of both daily and seasonal evapotranspiration of the basin. The Normal Difference Vegetation Index was compared against to the daily evapotranspiration of the basin to show the effect of vegetation on spatial distribution of daily evapotranspiration as shown in figure 4.5. The result of both the line graph and linear scatter plot shows the direct relationship between the NDVI and daily ET with the linear regression coefficient (R^2) value of 0.67.

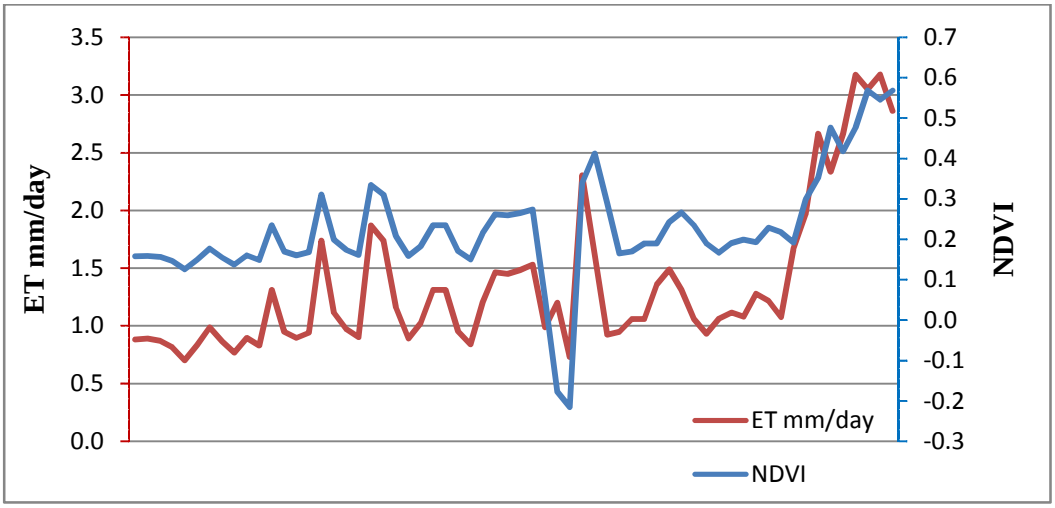

Figure 4.5. Line graph of NDVI and daily evapotranspiration

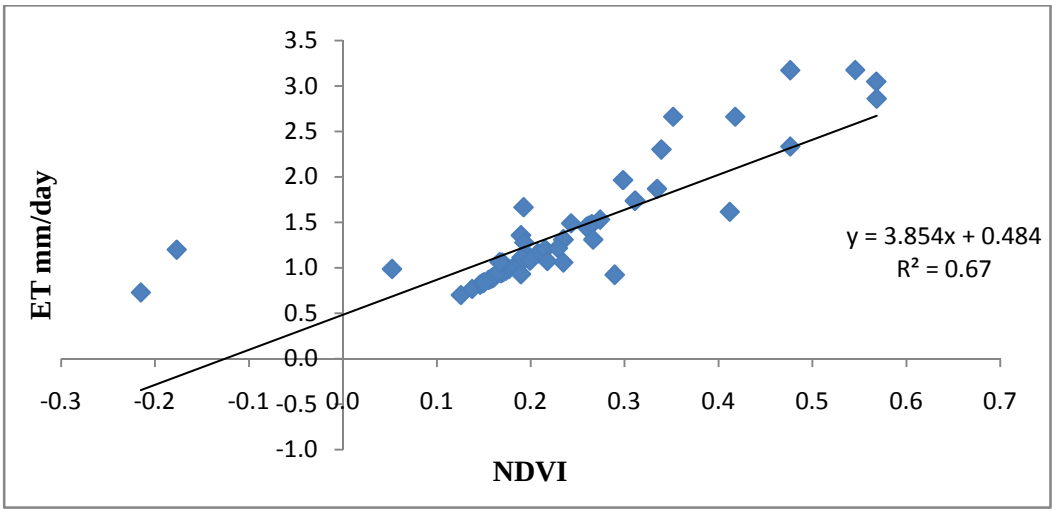

Figure 4.6. Scatter plot of NDVI and daily evapotranspiration

4.4. Validation of SEBAL Daily ET with Penman-Monteith Daily ETo

The Surface Energy Balance Algorithm for Land (SEBAL Model) gives a satisfactory result on different countries due to its internal calibration for the different satellite images. According to Bastiaanssen et al. (2005) SEBAL model has been validated under a range of soil wetness and plant community conditions and the typical accuracy at field scale is 85% for a day basis and it increases to 95% on a seasonal basis. The accuracy of annual evapotranspiration of large watersheds was found to be 96% on average.

4.4.1. SEBAL Daily ET with Penman-Monteith Reference ET

Despite of the ground truth data of actual ET was not available for validation, the comparison made between Penman-Monteith daily reference ET and SEBAL daily ET results for this study. The line graph trend analysis of Penman-Monteith reference ET and SEBAL daily evapotranspiration (see figures 4.7, 4.9 and 4.11) show the direct relationship between observed and simulated evapotranspiration values of the basin. Similarly, the linear regression analysis between the Penman-Monteith reference evapotranspiration and SEBAL daily ET gives a strong relationship between observed and simulated evapotranspiration values with the linear regression coefficient (R^2) of 0.85, 0.8 and 0.77 as shown on figure 4.8, 4.10 and 4.12 respectively.

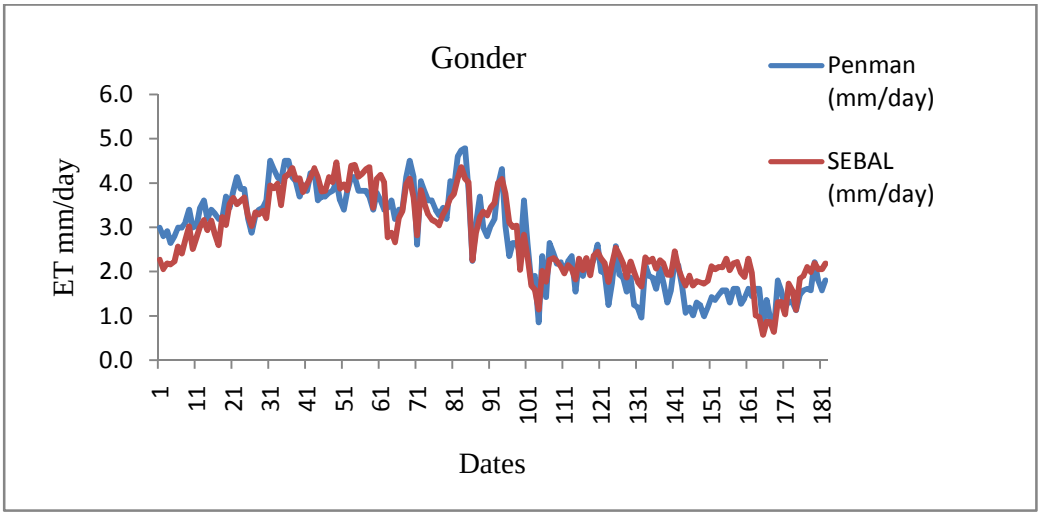

Figure 4.7. Line graph of SEBAL daily ET and Penman-Monteith ETo at Gonder station

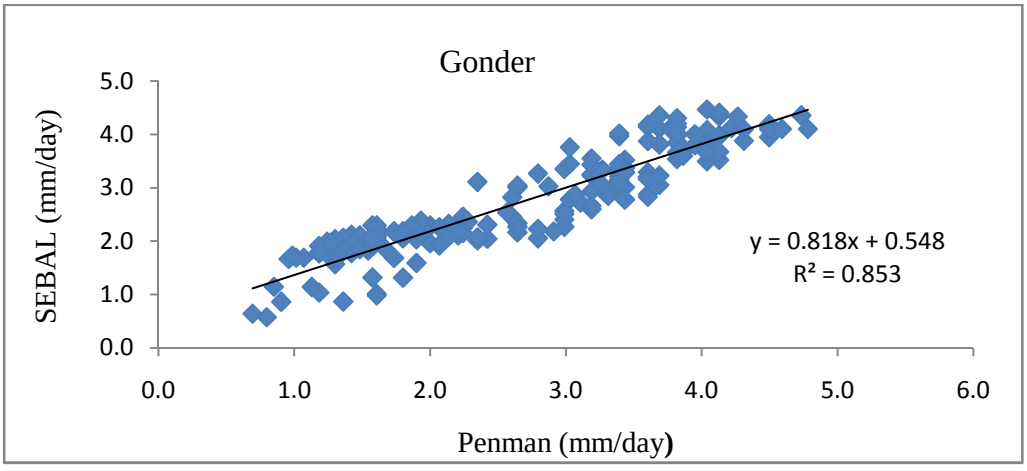

Figure 4.8. Scatter plot between SEBAL daily ET and Penman-Monteith ETo at Gonder station

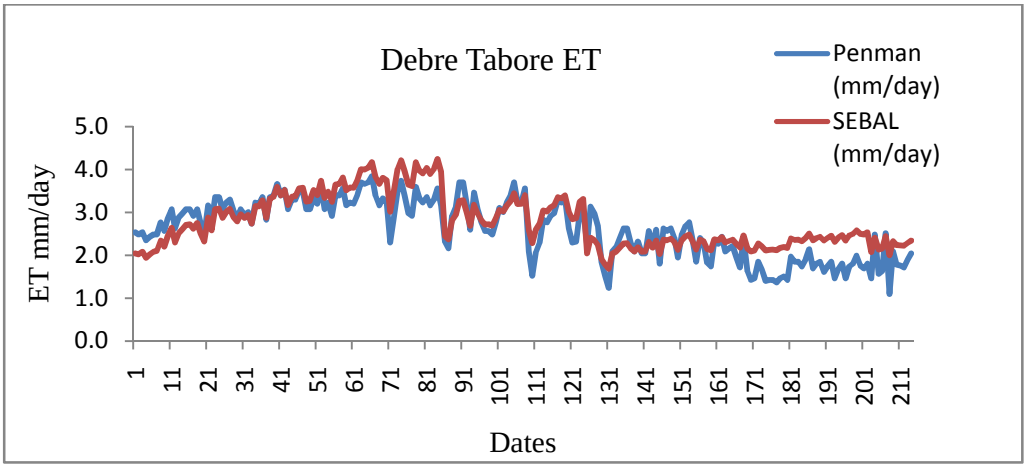

Figure 4.9. Line graph of SEBAL daily ET and Penman-Monteith ETo at Debre Tabore station

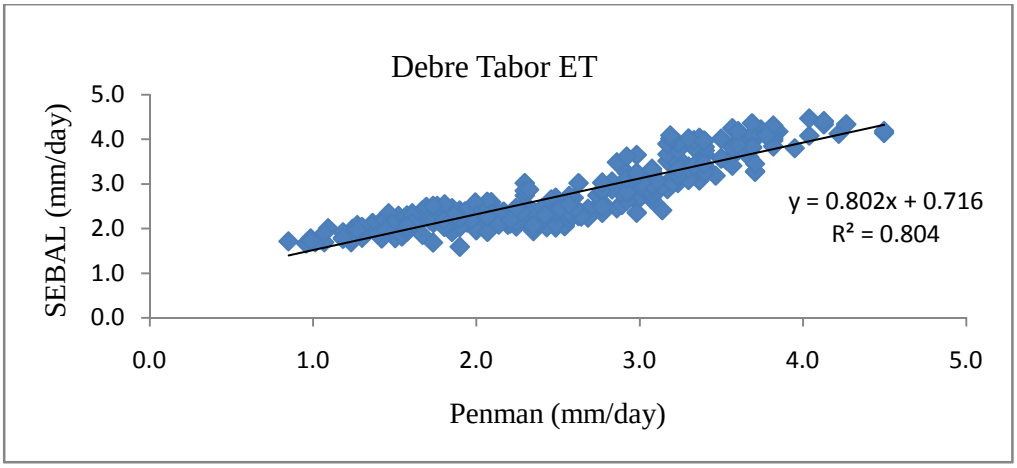

Figure 4.10. Scatter plot between SEBAL daily ET and Penman-Monteith ETo at Debre Tabore station

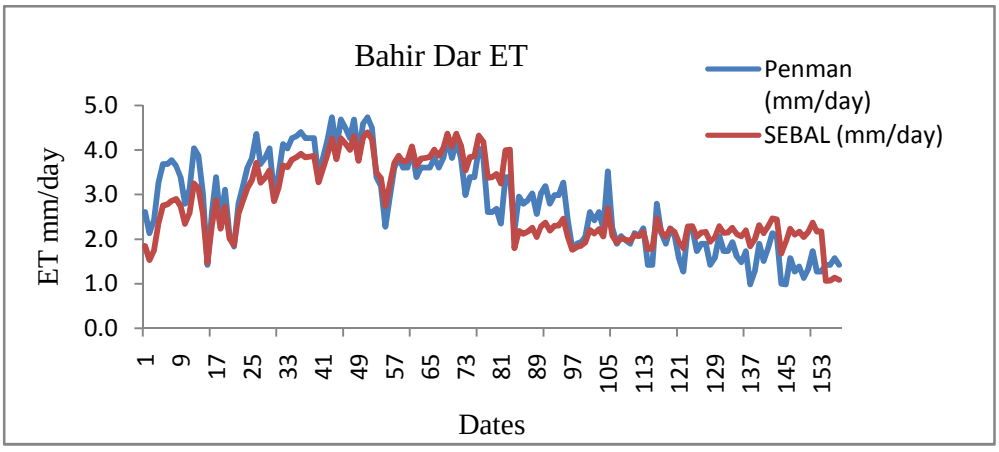

Figure 4.11. Line graph between SEBAL daily ET and Penman-Monteith ETo at Bahir Dar station

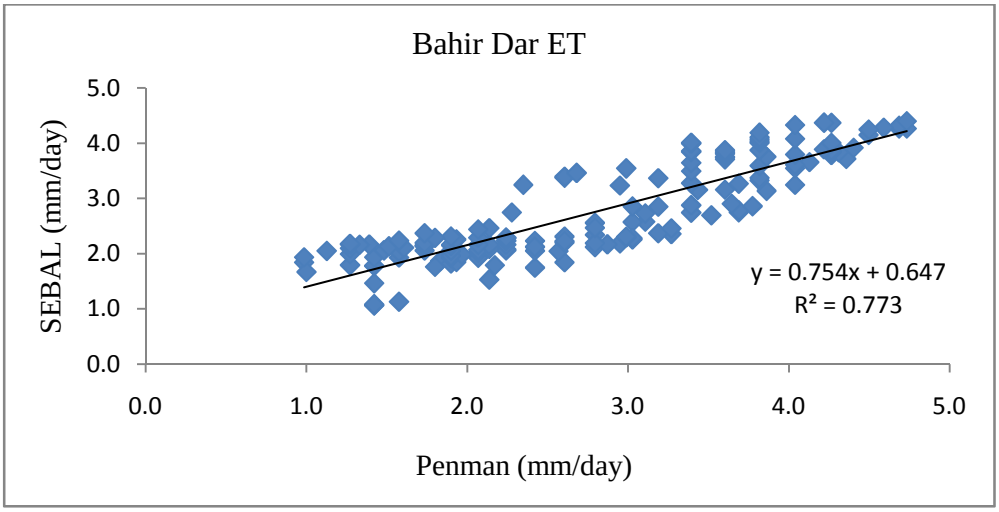

Figure 4.12. Scatter plot between SEBAL daily ET and Penman-Monteith ETo at Bahir Dar station

CHAPTER 5 : CONCLUSION AND RECOMMENDATIONS

5.1. Conclusion

The fresh water used for domestic, irrigation agriculture and industry is scarce resource that needs to planned management and wise use in a sustainable manner. Lake Tana basin which found in northwest highland of Ethiopia has high potential for irrigation agriculture, hydroelectric power development and ecotourism. However, there is high water demand both by the government as well as the stockholders of the basin. Due to this, the water resource systems of the basin show variations in their accumulated flow, distribution and overall storage volume with time. The basic objective of this research was to estimate the daily and seasonal evapotranspiration of Tana basin and mapping its spatial distribution in different land use and land cover types. The Surface Energy Balance Algorithm for Land (SEBAL Model) was applied to three Landsat TM satellite images corresponding to November 18 and 27, 2011 to produce estimates of the actual evapotranspiration at 30×30m resolution for the satellite over pass time. Once the instantaneous ET was generated, it was extrapolated to the daily ET value and seasonal accumulated ET values using the evaporative fraction and the Penman Monteith reference evapotranspiration.

The daily Penman-Monteith reference evapotranspiration ET_0 which calculated from meteorological data of the basin was found as 4.3 mm/day. The actual evapotranspiration of the basin computed using SEBAL model ranges from 0 to 4.3 mm/day that observed on bare lands and water bodies of the basin, respectively. The large portion of the basin has the range of evapotranspiration between 1.3 to 2.3 mm/day which covered by agricultural crops and grasslands. The woody savanna grass lands have actual evapotranspiration of 2.4 to 2.8 mm/day and the maximum amount of daily actual evapotranspiration was measured on forest lands and water bodies of the basin which is about 2.9 to 4.3 mm/day. The dry season evapotranspiration of the basin also measured between 20 to 439 mm depth of water.

The spatial distribution of evapotranspiration is related to the distribution of vegetation in the basin. The eastern and western parts of the basin show lower evapotranspiration corresponding to their little or no vegetation cover. However, the (southern) downstream of the Lake has relatively higher evapotranspiration due to its relatively dense vegetation cover. Finally, the daily SEBAL ET was compared to the Penman Monteith daily reference ET and the linear regression analysis shows that daily ET of the SEBAL model has a strong relationship with Penman-Monteith reference evapotranspiration of the study area.

5.2. Recommendations

Remote Sensing approach can provide more efficient and economically feasible outputs with relatively high spatial and temporal resolution than point measurements for evaluation of both surface and atmospheric processes including evapotranspiration. Based on the present study, the following important recommendations are made for the future researches those will conduct in the study area:

- Additional researches are essential with the integration of two or more surface energy balance models and some ground based models like scentillation method, eddy covariacne method and Bown ratio methods to make accurate estimation of the basin evapotranspiration.
- The evapotranspiration of the basin should be estimated based on long time series meteorological and remote sensing data.
- The basin evapotranspiration should be estimated using high resolution satellite imges of such as SPOT, IKONOS etc.

References

Abeyou Wale (2008). Hydrological Balance of Lake Tana, Upper Blue Nile Basin, Ethiopia. MSc Thesis ITC. Enschede, Netherlands.

Adediji, T. A., Oladosu, R.O., Jegede, O.O. and Sunmonu, A.L. (2007). Bowen ratio Estimation of surface energy fluxes in a humid tropical agricultural site, Ile-Ife, Nigeria. Indian Journal of Radio and Space physics. Vol, 36: 213-218.

Aduah, S.M., Mantey, S. and Amihyiah, A.E. (2011). Remote Sensing and GIS in Modeling Actual Evapotranspiration: A Case Study Using the Triangle Method in Tarkwa, South West Ghana. European Journal of Scientific Research. 62(2):257-266.

Allen, R.G., Pereira, L.S., Raes, D., Smith, M. (1998). Crop Evapotranspiration Guidelines for Computing Crop Water Requirements. FAO Irrigation and Drainage Paper. No. 56. Rome, Italy.

Allen, R.G., Tasumi, M., Trezza, R. and Waters, R. (2001). SEBAL (Surface Energy Balance Algorithms for Land): Advance Training and Users Manual, Idaho Implementation, version 1.

Allen, R. G., Tasumi, M., and Trezza, R. (2007). Satellite-based energy balance for mapping evapotranspiration with internalized calibration (METRIC) Model Applications. Journal of Irrigation and Drainage Eng., 133:4(380).

Allen, R., Irmak, A., Trezza, R., Hendrickx, M. H., Bastiaanssen, W. and Kjaersgaard, J.(2011). Satellite-based ET estimation in agriculture using SEBAL and METRIC. Hydrol. Process. 25, 4011–4027.

Almhab, A.A. (2009). Estimation of Regional Evapotranspiration using Remote Sensing Data in Arid Areas. PhD Dissertation, Technology University of Malaysia.

Ateawung, N.J. (2010). A GIS Based Water Balance study of Africa. MSc Thesis, for Master of Physical Land Resources, Universiteit Gent, Vrije Universiteit Brussel, Belgium.

Ayenew, T.(2003). Evapotranspiration estimation using thematic mapper spectral satellite data in the Ethiopian rift and adjacent highlands. Journal of Hydrology. 279 83–93.

Bakker, H.W., Janssen, F.L., Weir, C.J., Gorte, H.G., Pohl, C., Woldai, T., Horn, A.J. and

Reeves, V.C. (2000). Principles of Remote Sensing: An Introductory Text Book. ITC, Enschede, Netherlands.

Barlow, M. (2001). Blue Gold: The Global Water Crisis and the Commodification of the World's Water Supply. Council of Canadians Chair, IFG Committee on the Globalization of Water, Canada.

Bastiaanssen, W.G.M. (1995). Regionalization of surface flux densities and moisture indicators in composite terrain: A remote sensing approach under clear skies in Mediterranean climate. PhD Thesis, Landbouwuniversiteit Wageningen.

Bastiaansssen, W.G.M., Menenti, M., Feddes, R.A., Holtslag, A.A.M.(1998a). A remote sensing surface energy balance algorithm for land (SEBAL) 1. Formulation. J. Hydrol. 212–213, 198–212.

Bastiaansssen, W.G.M., Pelgrum, H., Wang, J., Ma, Y., Moreno, J.F., Roerink, G.J., Wal van der, T.(1998b). A remote sensing surface energy balance algorithm for land (SEBAL). 2. Validation. J. Hydrol. 213–229.

Bastiaanssen, W.G.M. and Mekonnen, G.M. (2000). A New Simple Method to Determine Crop Coefficients for Water Allocation Planning from Satellites: Results from Kenya. Irrigation and Drainage Systems, 14(3): 237-256.

Bastiaanssen, W.G.M., Noordman, E.J.M., Pelgrum, H., Davids, G., Allen, R.G. (2005). SEBAL for spatially distributed ET under actual management and growing conditions. J. Irrig. Drain. Eng. 131, 85–93.

Baumann, P.R.(2009). History of Remote Sensing Satellite Imagery. No.II. Available at: http://www.oneonta.edu/faculty/baumanpr/geosat2/RS%20History%20II/RSHistory-Part-2.html

Blumenfeld, S., Lu, C., Christophersen, T. and Coates, D. (2009). Water, Wetlands and Forests. A Review of Ecological, Economic and Policy Linkages. Secretariat of the Convention on Biological Diversity and Secretariat of the Ramsar Convention on Wetlands, Montreal and Gland. CBD Technical Series No. 47.

Burnett, B. (2007). A Procedure for Estimating Total Evapotranspiration using Satellite-Based Vegetation Indices with Separate Estimates from Bare Soil. MSc Thesis, University of Idaho. Moscow, Idaho.

Brutsaert, W. (1982). Evaporation into the atmosphere. Reidal, Dordrecht.

Courault, D., Seguin, B. and Olioso, A. (2005). Review on Estimation of Evapotranspiration from Remote Sensing Data: From Empirical to Numerical Modeling Approaches. Irrigation and Drainage Systems. 19: 223-249.

Effendi, I. (2012). Evapotranspıratıon in Dry Climate Area: Comparing Remote Sensing Techniques with Unsaturated Zone water flow simulation. MSc Thesis, International Institute for Geo-Information Science and Earth Observation, Enschede, The Netherlands.

FAO (2006). Crop Evapotranspiration (guidelines for computing crop water requirements): Irrigation and Drainage Paper No. 56.

Giridhar, S.S. and Suneel, P. (2014). Net Radiation Estimation from a Remotely Sensed Data Using SEBAL Model. International Journal of Engineering Research Issue Special.3: 2347- 5013.

Goulden, M. L., Munger, J.W., Fan, S.M., Daube, B.C. and Wofsy, S.C. (1996). Measurements of carbon sequestration by long-term eddy covariance: Methods and a Critical evaluation of accuracy. Global Change Biology. 2: 169-182.

Harvey, F. (2008). A Primer of GIS: Fundamental Geographic and Cartographic Concepts. The Guilford Press, New York London.

Hassan S.M.H.,Shariff, A.R.M. and Amin, M.S.M.(2008). A Comparative Study of Evapotranspiration Calculated from Remote Sensing, Meteorological and Lysimeter data. **In:** Proceedings of the 3rd International Conference on Water Resources and Arid Environments, Alazhari University, Khartoum North-Sudan.

IPCC (1998). Intergovernmental Panel on Climate Change (IPCC). Available at: http://www.ipcc.ch/

Kebede, S., Travi,Y., Alemayehu, T. and Marc, V. (2006). Water Balance of Lake Tana and its sensitivity to fluctuations in rainfall, Blue Nile Basin, Ethiopia. Journal of Hydrology 316 : 233–247.

Kosa, P. (2011). The Effect of Temperature on Actual Evapotranspiration based on Landsat 5 TM Satellite Imagery, Evapotranspiration, Prof. Leszek Labedzki (Ed.), ISBN: 978-953-307-251-7, InTech, Available from: http://www.intechopen.com/books/evapotranspiration/the-effect-of-temperature-on-actualevapotranspiration-

Konecny, G. (2003). Geoinformation: Remote sensing, photogrammetry and geographic information systems. 1st Edition. Taylor & Francis Press, London.

Latha, C.J., Saravanan, S. and Palanichamy.K. (2010). A Semi-Distribute Water Balance

Model for Amaravathi Rver Basin using Remote Sensing and GIS. International Journal of Geomtics and Geosciences. 1(2):252-254.

Lillesand, T.M. and Kiefer, R. (1993). Remote Sensing and Image Interpretation. 3rd Edition John Villey, New York.

Lillesand, M. and Kiefer, R.W. (2004). Remote Sensing and Image Interpretation. Fourth Edition. John Willy & Sons Inc. Newark, Chechister, Wenheim, Brisbane, Singapore and Toronto.

Li, Z., Tang, R., Wan, Z., Bi, Y., Zhou, C., Tang, B., Yan, G. and Zhang, X. (2009). A Review of Current Methodologies for Regional Evapotranspiration Estimation from Remotely Sensed Data. Journal of Sensors. 9: 3801-3853.

Liou, A.Y. and Kar, K.S. (2014). A Review of Evapotranspiration Estimation with Remote Sensing and Various Surface Energy Balance Algorithms. Journal of Energies. 7: 2821-2849.

McCartney, M., Alemayehu, T., Shiferaw, A., Awulachew, S. B. (2010). Evaluation of current and future water resources development in the Lake Tana Basin, Ethiopia. IWMI, Colombo, SriLanka.

McCornick P.G., Kamara A.B. and Girma Tadesse. (eds). (2003). Integrated water and land management research and capacity building priorities for Ethiopia. Proceedings of a MoWR/EARO/IWMI/ILRI international workshop held at ILRI, Addis Ababa, Ethiopia, 2–4 December 2002. IWMI (International Water Management Institute), Colombo, Sri Lanka, and ILRI (International Livestock Research Institute), Nairobi, Kenya.

Melkamu Amare (2005). Reservoir operation and establishment of reservoir rule for lake Tana. Unpublished MSc Thesis, Addis Ababa University. Addis Ababa, Ethiopia.

Mendonca, J.C., Sousa, E.F., Andre, B.G.R., Bernardo Barbosa da Silva, B.B. and Ferreira, J.N., (2012). Assessment of Evapotranspiration in North Fluminense Region, Brazil, Using Modis Products and Sebal Algorithm, Evapotranspiration. Available from: http://www.intechopen.com/books/evapotranspiration-remote-sensing-and-modeling/assessment-ofevapotranspiration-

Miralles, D. G. (2011). Evaporation in the Global Water Cycle: Analysing Land Evaporation Using Satellite Observations. PhD Dissertation, Vrije Universiteit Amsterdam. Madrid, Spain.

Moulick, N.H. and Moumita Ghosh, M. (2013). Digital Image Processing Techniques for

Detection and Satellite Image Processing. International Refereed Journal of Engineering and Science (IRJES).Vol-2. ISSN (Online) 2319-183X, (Print) 2319-1821.

Mulushewa Zemede (2013). Hydrological Impacts of Climate Change on Lake Tana Water Balance. MSc Thesis, International Institute for Geo-Information Science and Earth Observation, Enschede, Netherland.

Mussa Kurkura (2011). Water Balance of Upper Awash Basin Based on Satellite Derived Data (Remote Sensing) . MSc Thesis, Addis Ababa University, Addis Ababa, Ethiopia.

Oberg, J. W. and Melesse, M.A. (2006). Evapotranspiration dynamics at an ecohydrological restoration site: An Energy Balance and Remote Sensing Approach. Journal of the American Water Resources Association. No. 04131:565-580.

Pelgrum, H. and Bastiaanssen, W. (2006). Remote sensing studies of Tana-Beles Sub-Basins. WaterWatch Remote Sensing Services. Avialable at: www.waterwatch.nl

Perez, P.J., Castellvi, F., Rosell, J.I., Ibanez, M. (1999). Assessment of reliability of Bowen ratio method for partitioning fluxes. Agric.For. Meteorol. 97(3):141-150.

Reddy, A.M. (2008). Textbook of Remote Sensing and Geographical Information Systems. 3rd Edition. BS Publications. Hyderabad, India.

Schowengerdt, R. A.(2007). Remote Sensing: Models and Methods for Image Processing. 3rd Edition. Academic Press.

Seleshi Bekele, Yilma, A. D., Loulseged, M., Loiskandl, W., Ayana, M., Alamirew, T. (2007). Water Resources and Irrigation Development in Ethiopia. Colombo, Sri Lanka: International Water Management Institute (IWMI). Working paper 123.

Setegn, G., Srinivasan, R. and Dargahi, B.(2008). Hydrological Modelling in the Lake Tana Basin, Ethiopia Using SWAT Model. The Open Hydrology Journal. 2: 49-62

Seth, S. M., Jain, S. K. and Jain, M. K.(1996). Remote sensing and GIS application studies at national institute of hydrology. National Institute of Hydrology. Roorkee 247667.

Shiklomanov, A. I. (1998). World Water Resources: A New Appraisal and Assessment for the 21st century. A Summary of the Monograph World Water Resources. International Hydrological Programme, UNESCO, Milton Keynes, UK.

SMEC (2008). Hydrological Study of the Tana-Beles sub-basins. Addis Ababa, Ethiopia.

Tamiru Alemayehu (2014). Modeling and Analysis of Lake Tana Sub Basin Water Resource

Systems, Ethiopia. PhD Dissertation, University of Rostock.

Tegegne Molla (2006). Estimation of Evapotranspiration for Irrigation Performance Assessment Using Satellite Remote Sensing at Kobo Valley Irrigation Project, Northern Ethiopia. MSc Thesis, Addis Ababa University, Addis Ababa, Ethiopia.

Urama, C.K. and Ozor, N. (2010). Impacts of climate change on Water Resources in Africa:The role of adaptation. African Technology Policy Studies Network (ATPS).

Verma, S.B., Rosenberg, N.J., Blad, B.L. (1978). Turbalaent exchange coefficients for sensible heat and water vapour advective conditions. Journal of Applied Meteorology. 17:330-338.

Wang, Q., Sun, Z., Matsushita, B. and Watanabe, M. (2011). A Simple Remote Sensing Evapotranspiration Model (Sim-ReSET) and its Application. InTech. Available at: http://www.intechopen.com/books/evapotranspiration/asimple-remote-sensing-evapotranspiration-model-sim-reset-and-its-application

Weligepolage, K. (2005). Estimation of Spatial and Temporal Distribution of Evapotranspiration by Satellite Remote Sensing. MSc Thesis, International Institute for Geo-Information Science and Earth Observation, Enschede, The Netherlands.

Yan, H., Wang, S.Q., Billesbach, D., Oechel, W., Zhang, J.H., Meyers, T., Martin, T.A., Matamala, R., Baldocchi, D., Bohrer, G., Dragoni, D. and Scott, R. (2012). Global estimation of evapotranspiration using a leaf area index-based surface energy and water balance model. Journal of Remote Sensing of Environment. 124: 581-595.

Yihun Dile (2009). Hydrological Modeling to Assess Climate Change Impact at Gilgel Abay River, Lake Tana Basin, Ethiopia. MSc Thesis, Division of Water Resources Engineering, Lund University, Sweden.

Yohannis Daniel (2007). Remote sensing based assessment of water resource potential for Lake Tana. Unpublished MSc Thesis Civil Engineering, Addis Ababa University.

Appendix

Coordinate System: Projected, UTM , Zone 37N

Datum: WGS 1984

Table 1. Sample GPS points in the Tana Basin

No.	Longitude (m)	Latitude (m)	Land Use Type
1	333518	1376456	Cultivated land
2	336831	1376836	forest land
3	333904	1376841	Cultivated land
4	334262	1377571	Cultivated land
5	334459	1378136	Bare land
6	334633	1378683	Bare land
7	335385	1378695	Cultivated land
8	333416	1381049	Cultivated land
9	330895	1391887	forest land
10	330881	1391917	forest land
11	330969	1392154	forest land
12	332852	1393279	Gonder town
13	333979	1394918	Gonder town
14	348130	1324859	Plantation
15	348051	1325022	Plantation
16	348061	1325133	Plantation
17	348235	1325737	Cultivated
18	349076	1325800	Bare land
19	348877	1325939	Bare land
20	342690	1302454	Hamusit
21	347978	1360093	forest land
22	348076	1360557	forest land
23	347992	1361332	forest land
24	346722	1362906	Cultivated land
25	345823	1363783	Cultivated land